Joule

CellPress

Article

Pathways to reduce the energy cost of carbon monoxide electroreduction to ethylene

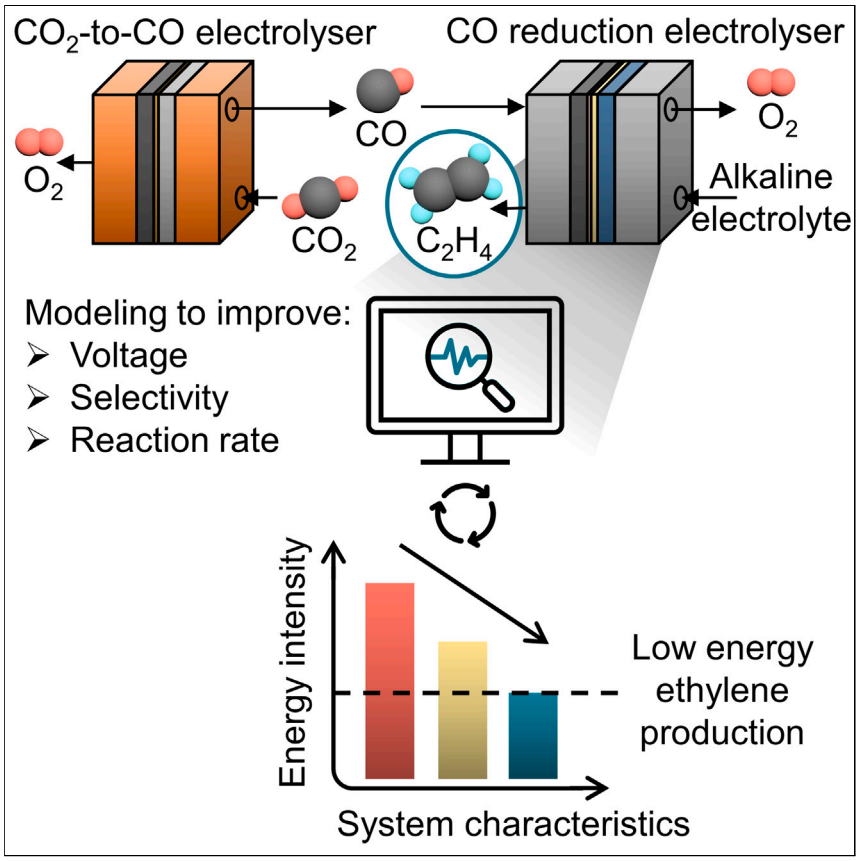

One promising approach to produce the highly desirable ethylene from CO_2 at high CO_2 utilization is the use of a cascade system, wherein CO_2 is first converted to CO followed by CO conversion to ethylene in an alkaline electrolyzer. Alkayyali and co-authors develop a computational model to survey the system properties of the currently underperforming alkaline electrolyzer. Through multi-parameter optimization, several properties are identified for future research to produce ethylene at low energy through the cascade system.

Tartela Alkayyali, Mohammad Zargartalebi, Adnan Ozden, ..., Aimy Bazylak, Edward H. Sargent, David Sinton

sinton@mie.utoronto.ca

Highlights

A model of a membrane electrode assembly electrolyzer is built and validated

CO reduction is characterized in terms of operation and voltage distribution

Taguchi optimization is employed to improve the CO-to-ethylene energy intensity

Progress in kinetics, component properties, and operational conditions are needed

Alkayyali et al., Joule *8*, 1–23
May 15, 2024
https://doi.org/10.1016/j.joule.2024.02.014

Please cite this article in press as: Alkayyali et al., Pathways to reduce the energy cost of carbon monoxide electroreduction to ethylene, Joule (2024), https://doi.org/10.1016/j.joule.2024.02.014

Joule

CellPress

Article

Pathways to reduce the energy cost of carbon monoxide electroreduction to ethylene

Tartela Alkayyali,[1] Mohammad Zargartalebi,[1] Adnan Ozden,[1] Fatemeh Arabyarmohammadi,[1] Roham Dorakhan,[2] Jonathan P. Edwards,[1] Feng Li,[1] Ali Shayesteh Zeraati,[1] Mengyang Fan,[1] Aimy Bazylak,[1] Edward H. Sargent,[2] and David Sinton[1,3,*]

SUMMARY

CO_2-to-CO conversion, followed by CO to value-added products, shows promise as a high-CO_2 utilization strategy. However, it is necessary to continue to reduce the energy intensity of CO electrolyzers. Modeling can untangle the highly coupled nature of these electrolyzers and thereby accelerate their optimization. Here, we develop a CO electrolyzer model, which we compare with experiments, and evaluate how it might be possible to attain CO to ethylene (C_2H_4) with the energy intensity approaching 110 GJ tonne^{-1} C_2H_4, then further to an 80 GJ tonne^{-1} C_2H_4 target. The model identifies targets and specifications for each component, with the ultimate target requiring continued progress in increasing cathodic catalyst selectivity, thin anion exchange membranes (<25 μm), improved ion exchange capacity (1.7–3.4 mmol/g), enhanced anode activity (>56% overpotential reduction) and thickness (100–400 μm), and optimized operation (1–4 M KOH at 25°C–75°C) at >300 mA cm^{-2}.

INTRODUCTION

Carbon dioxide utilization technologies can reduce CO_2 emissions and provide renewable paths to carbon-based fuels and products.[1,2] Ethylene (C_2H_4) is a particularly desirable CO_2 electroreduction product because it has a large market size,[3,4] it is the most-produced organic compound from fossil fuels,[5] and its current production methods are energy and carbon intensive.[6]

Electrochemical CO_2 reduction reaction (CO_2RR) reactors have improved rapidly with respect to energy efficiency (EE; the fraction of the applied full-cell potential that goes toward making the target product relative to its standard cell potential) and rate.[5,7–9] However, many prior studies suffer reactant CO_2 loss to carbonates[8,10]: CO_2 reacts with hydroxide ions (OH^-) under alkaline conditions to form bicarbonate and carbonate ions; these ions cross the anion exchange membrane (AEM) to the anode and are oxidized back to CO_2.[11] This CO_2 combines with anode-produced O_2 (Figure 1A), resulting in a mixture that is costly to separate.[26] When carbonates are the major charge carriers, the upper limit of single-pass CO_2-to-C_2H_4 conversion is 25%.[10] Carbonate formation in CO_2RR membrane electrode assembly (MEA) electrolyzers also results in large pH gradients and Nernstian losses, leading to a ~35% higher energy intensity (i.e., the amount of energy needed to operate the electrolyzer and its required upstream and downstream processes, such as anode and cathode separation, for every tonne of product produced; see Note S1) compared with carbonate-free systems.[13]

CONTEXT & SCALE

Rising CO_2 emissions motivate the development of CO_2 mitigation technologies. The electroreduction of CO_2 to ethylene, the most-produced organic compound (201 Mt in 2020), has potential to contribute to decarbonizing a significant commodity chemical. However, direct CO_2 electrolysis suffers from carbonate formation. A promising alternative is CO_2 electrolysis in a two-step process: CO_2 to CO, followed by CO to ethylene. The first, simpler two-electron reaction already benefits from electrified routes with relatively modest energy consumption. The second step, carried out in an alkaline electrolyzer, requires further improvements to make the overall process energy efficient. The multi-physics nature of this process makes it difficult to optimize experimentally. For this reason, we here develop a computational model of the CO electrolysis system, assess the opportunities to improve performance, and identify the advances needed to reduce the electrolyzer input electricity demand.

Please cite this article in press as: Alkayyali et al., Pathways to reduce the energy cost of carbon monoxide electroreduction to ethylene, Joule (2024), https://doi.org/10.1016/j.joule.2024.02.014

An emerging approach is the two-step, or cascade, system of CO_2-to-CO conversion followed by CO to high-value products in a low temperature alkaline CO reduction reaction (CORR) electrolyzer (Figure 1B).[13,27,28] Unlike CO_2, carbon monoxide does not spontaneously react with OH^- in alkaline solutions. Over the last two decades, CO_2-to-CO electrolyzers have advanced greatly,[27,29] with the highest EEs (>70%) being achieved in high temperature solid oxide electrolyzer (SOEC) systems.[30]

Considering the overall CO_2-to-C_2H_4 process, we assess here the progress required to achieve an ambitious target of 110 GJ tonne^{-1} C_2H_4, and then the requirements of a further reduction to 80 GJ tonne^{-1} C_2H_4[31] (which, in light of the lower heating value of C_2H_4,[13] 48 GJ tonne^{-1} C_2H_4, correspond to a process efficiency of >44% and >60%, respectively). We implement an energy analysis model (Note S1), based upon models reported in our previous work,[3,13,31] to compare the energy intensity of the electrochemical CO_2-to-C_2H_4 conversion via the direct CO_2RR system or via the cascade system (Figure 1C; see also Note S2 for energy analysis of other low-CO_2-crossover CO_2RR systems). If the direct CO_2RR system was to operate at optimistic single-pass conversion (SPC; the fraction of input reactant converted to the target product relative to the input reactant amount) conditions, the overall energy intensity would be 224 GJ tonne^{-1} C_2H_4 (Table S1). For the cascade system, the current best literature benchmarks for the CO_2-to-CO step[13] and the CORR step[12] achieve 26 and 140 GJ tonne^{-1} C_2H_4, respectively, yielding an overall energy intensity of 166 GJ tonne^{-1} C_2H_4. In all cases, the dominant energy intensity in both the direct and cascade systems is electrolyzer electricity.[32] Thus, the prospect of such systems hinges on improving the EE, particularly in the CORR step (currently <28%[13,28]).

To establish guidelines for the energy intensity requirements of the cascade system, we survey a range of operating conditions in each step. In the case of CO_2 conversion to CO, operating at >90% electrical efficiency[33] and considering the lower heating value of CO (~10 GJ tonne^{-1} CO[34]), the energy intensity required for this conversion could be as low as 11 GJ tonne^{-1} CO, or 22 GJ tonne^{-1} C_2H_4, which we consider as an ambitious long-term target for the CO_2-to-CO step in the remainder of this work (Note S1). We find that this energy intensity would be achieved with ~100% CO Faradaic efficiency (FE; the fraction of input electrons successfully participating in generating the target product), >57% CO_2 SPC, and <1.1 V (Figures 1D, S1, and S2). Achieving such a level of performance would necessitate further improvements, mainly in SPC, relative to the current best SOEC demonstration[13] (Table S1).

Given the larger energy intensity associated with the second step of the cascade, we focus here on the advances required in the CORR step. A variety of FE and full-cell potential targets for C_2H_4 production from CORR have been reported,[3,31] reflecting the requirement of >53% C_2H_4 EE. Through our energy analysis model, we find that a higher CO SPC enables less restrictions on C_2H_4 FE and full-cell potential targets (Figures 1E, S3, and S4). While flow cells can provide high total current densities (Figure 1F), and thus SPC, flow cells require high full-cell potentials due to the large ohmic drop caused by the catholyte, limiting their EE.[35] The MEA approach to CORR is more promising due to the enablement of high EE and scalability. However, a minority of recent reports implement CORR in an MEA (Figure S5; Table S2) and C_2H_4 FE has yet to exceed 70% (Figure 1F).

Little information is provided in the literature regarding the sub-component materials and performance levels that could—when implemented in a full system—realize the targets required for low-energy CO to C_2H_4. Formal optimization of electrolyzers

[1]Department of Mechanical and Industrial Engineering, University of Toronto, 5 King's College Road, Toronto, ON M5S 3G8, Canada

[2]Department of Electrical and Computer Engineering, University of Toronto, 35 St. George Street, Toronto, ON M5S 1A4, Canada

[3]Lead contact

*Correspondence: sinton@mie.utoronto.ca

https://doi.org/10.1016/j.joule.2024.02.014

Please cite this article in press as: Alkayyali et al., Pathways to reduce the energy cost of carbon monoxide electroreduction to ethylene, Joule (2024), https://doi.org/10.1016/j.joule.2024.02.014

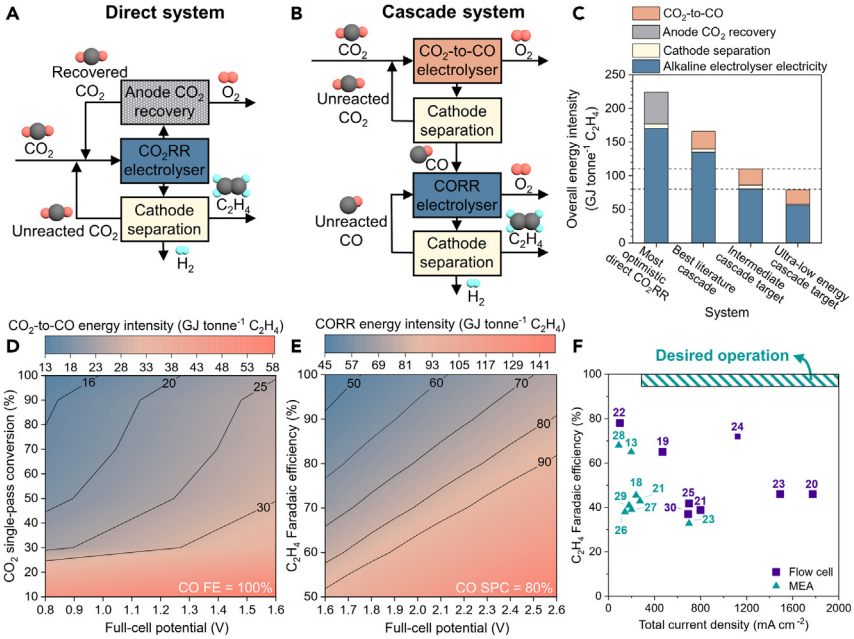

Figure 1. Energy analysis of carbon monoxide and ethylene electroproduction systems

(A) Schematic of a system in which ethylene is directly produced from CO_2 in an alkaline CO_2 reduction reaction (CO_2RR) electrolyzer. Other required processes are also indicated and color-coded according to their respective energy intensity values in (C).

(B) Schematic of a cascade system in which a CO_2-to-CO electrolyzer feeds an alkaline CO reduction reaction (CORR) electrolyzer that converts CO to ethylene. Other required processes are also indicated and color-coded according to their respective energy intensity values in (C).

(C) Overall energy intensity values of a direct system operating at the most optimistic CO_2RR single-pass conversion, a cascade system operating at current best literature metrics,[12] and target cascade systems (Table S1). The top dashed line indicates the intermediate overall target of 110 GJ tonne^{-1} C_2H_4, and the bottom dashed line indicates the ultra-low overall energy intensity target of 80 GJ tonne^{-1} C_2H_4 for the cascade system. Given that 1 mol of ethylene requires 2 mol of CO, the GJ tonne^{-1} C_2H_4 values reported for the CO_2-to-CO electrolyzer assume the production of 2 mol of CO. The CO_2-to-CO electrolyzer (here an SOEC as an example) energy intensity values include electrolyzer electricity, heating, and cathode separation.

(D) Energy intensity of the CO_2-to-CO electrolyzer (here an SOEC) at a CO Faradaic efficiency (FE) of 100%, 1,000 mA cm^{-2} total current density, and 800°C.

(E) CORR energy intensity at a CO single-pass conversion (SPC) of 80% and 300 mA cm^{-2} total current density.

(F) Current state-of-the-art for ethylene electroproduction through alkaline CORR flow cells and membrane electrode assemblies (MEAs).[12–25] Shaded region indicates favorable operating conditions (>94% C_2H_4 FE and >300 mA cm^{-2}). Labels indicate reference numbers.

through experiments is costly, time consuming, and cannot address the wide parameter space. Modeling is comparably high-throughput and can speed up experimental optimization. The emergence of CORR as an alternative route to C_2H_4 production motivates a comprehensive model of this process and a critical assessment of its performance within the cascade system.

Here, we develop a model of CORR to multi-carbon (C_{2+}) products in an MEA electrolyzer. In-house experiments are designed and performed to build and test the model, and literature data are used for comparison. We first apply the model to understand the cell potential distribution in the CORR MEA electrolyzer and analyze the local environment as different operating conditions are applied. We then quantify the effects of catalytic, geometric, and operational cell parameters on performance metrics (C_2H_4 FE, total current density, full-cell potential, and CO SPC). Using

Please cite this article in press as: Alkayyali et al., Pathways to reduce the energy cost of carbon monoxide electroreduction to ethylene, Joule (2024), https://doi.org/10.1016/j.joule.2024.02.014

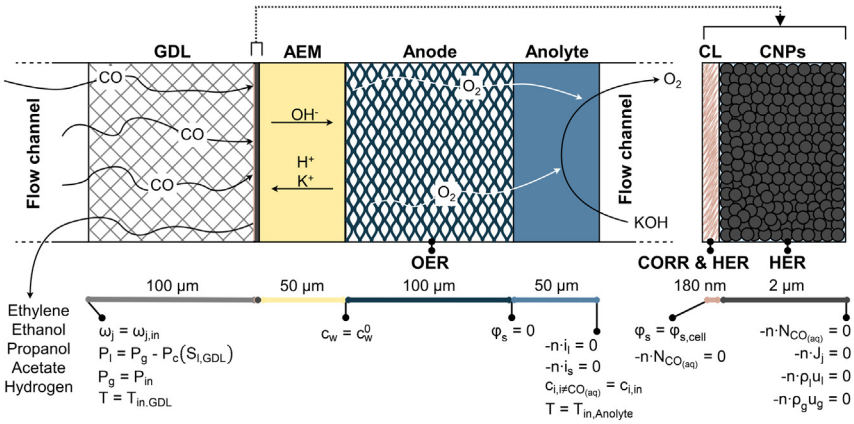

Figure 2. Model overview

A schematic illustration of the computational domain and the associated boundary conditions. The model reflects an alkaline CO reduction reaction (CORR) membrane electrode assembly electrolyzer in the order of a gas diffusion layer (GDL), a catalyst layer (CL), a layer of carbon nanoparticles (CNPs), an anion exchange membrane (AEM), an anode, and an anolyte. Flow channels are shown to clarify the inputs and outputs of the cell. Boundary conditions are indicated. CORR and the hydrogen evolution reaction (HER) are considered in the CL, while the CNPs are considered to participate in HER. The oxygen evolution reaction (OER) is considered at the anode.

multi-parameter optimization and analysis, we outline the advances in cell parameters required to minimize the energy intensity of C_2H_4 electroproduction via the CORR MEA electrolyzer.

RESULTS AND DISCUSSION

CORR model overview and validation

The model reflects the configuration of, and components within, high-performance MEA electrolyzers in the literature.[13,36] Inspired by established full-cell models for CO_2RR,[37–40] we employ a stationary, one-dimensional MEA electrolyzer model. The base case model is composed of a 100-μm polytetrafluoroethylene (PTFE) gas diffusion layer (GDL), a 180-nm copper catalyst layer (CL), a 2-μm carbon nanoparticle layer (CNP), a 50-μm AEM, a 100-μm IrO_2 on Ti mesh anode, and a 50-μm KOH anolyte (Figure 2; Table S3). The GDL, CL, and CNPs are assumed to have volume-averaged properties that are influenced by gas and liquid saturation levels. The CNPs layer is employed on the CL to increase electrical conductivity and achieve a geometrically uniform current distribution across the CL,[36,41] especially important given the insulating nature of the PTFE GDL. CO is supplied to the backside of the GDL and is transferred from the gas phase to the liquid phase at a thin liquid film wetting the CL and CNPs pores according to saturation characteristics.[37] Zero ionic flux is assigned at the GDL:CL interface, and no CO diffusion is assumed through the AEM. A negative full-cell potential is applied at the GDL:CL interface ($\varphi_{s,cell}$), while ground is set at the anode's right-hand side boundary.

CORR performed on a copper-based catalyst typically produces a mixture of products, and thus we consider the evolution of C_2H_4, ethanol, propanol, acetate, and hydrogen at the cathode as follows:

$$2CO + 6H_2O + 8e^- \rightarrow C_2H_4 + 8OH^- \quad \text{(Equation 1)}$$

$$2CO + 7H_2O + 8e^- \rightarrow C_2H_5OH + 8OH^- \quad \text{(Equation 2)}$$

Please cite this article in press as: Alkayyali et al., Pathways to reduce the energy cost of carbon monoxide electroreduction to ethylene, Joule (2024), https://doi.org/10.1016/j.joule.2024.02.014

$$3CO + 10H_2O + 12e^- \rightarrow C_3H_8O + 12OH^- \quad \text{(Equation 3)}$$

$$2CO + 3H_2O + 4e^- \rightarrow CH_3CO_2^- + 3OH^- \quad \text{(Equation 4)}$$

$$2H_2O + 2e^- \rightarrow H_2 + 2OH^- \quad \text{(Equation 5)}$$

Simultaneously, alkaline and acidic oxygen evolution reactions (OERs) are considered at the anode, respectively, as follows:

$$4OH^- \rightarrow O_2 + 2H_2O + 4e^- \quad \text{(Equation 6)}$$

$$2H_2O \rightarrow O_2 + 4H^+ + 4e^- \quad \text{(Equation 7)}$$

and water dissociation is considered throughout the cell:

$$H_2O \leftrightarrow H^+ + OH^- \quad \text{(Equation 8)}$$

To test and calibrate the model, we develop a similarly constructed experimental MEA electrolyzer for CORR (see supplemental experimental procedures) and analyze the product distribution at different applied full-cell potentials. Using the experimental results, we fit the kinetic parameters of the cathodic reactions (Note S3; Figure S6). The model and experiments show good agreement on partial current density at various applied potentials, with a root mean squared error[42] of 8.3 mA cm^{-2} for C_2H_4, 1.8 mA cm^{-2} for ethanol, 1.9 mA cm^{-2} for propanol, 0.8 mA cm^{-2} for acetate, and 2.3 mA cm^{-2} for H_2 when compared with experimentally provided values between 2.2 and 3.0 V. The model results are further compared with experimental results obtained at various KOH concentrations (Figure S7). The model is also validated using experimental results from a literature report of a CORR MEA electrolyzer[43] (Figure S8).

Characterizing the CORR MEA electrolyzer

To improve the performance of CORR MEA electrolyzers, their operation and local conditions must be first understood. With the full-cell potential being a large contributor to the electrolyzer electricity cost, we sought to analyze the breakdown of the voltage in the system as a function of operating conditions (Figure 3A). The components of the full-cell potential are calculated according to recommended guidelines (Note S4).[37,44] We also apply a voltage diagnostic tool[45] (Note S5) to experimentally measure the full-cell potential components at the same MEA setup and conditions used in the base case model. The results from the model and the voltage diagnostic show good agreement as a function of current density (Figure S9). Through the model, the thermodynamic potential is observed to be between 1.05 and 1.17 V, as it depends on the product distribution. Lower full-cell potentials could be achieved by strategically selecting organic oxidation reactions with low thermodynamic potentials.[13,24,46–49] However, such alternate anodic reactions are less well defined, their reactants/intermediates/products could affect the cathode, they require additional reactants to be sourced, and realizing value from the anodic products would require additional product separation processes and associated costs.[4,46] Therefore, the scope of this work is limited to OER at the anode. With OER, the obtained anode kinetic overpotential is between 0.23 and 0.31 V. The cathode kinetic overpotential can be considered as the aggregate contribution of all produced products at the cathode (Figure 3A). The cathode kinetic overpotential contribution of each product correlates with its FE (Figure S10), emphasizing that CORR MEA electrolyzers are at a disadvantage when the hydrogen evolution reaction (HER) competes with C_{2+} products for electrons (e.g., at 100–300 mA cm^{-2}, H_2 consumes 0.13–0.19 V and C_2H_4 consumes 0.44–0.60 V, while at 450 mA cm^{-2}, H_2

Please cite this article in press as: Alkayyali et al., Pathways to reduce the energy cost of carbon monoxide electroreduction to ethylene, Joule (2024), https://doi.org/10.1016/j.joule.2024.02.014

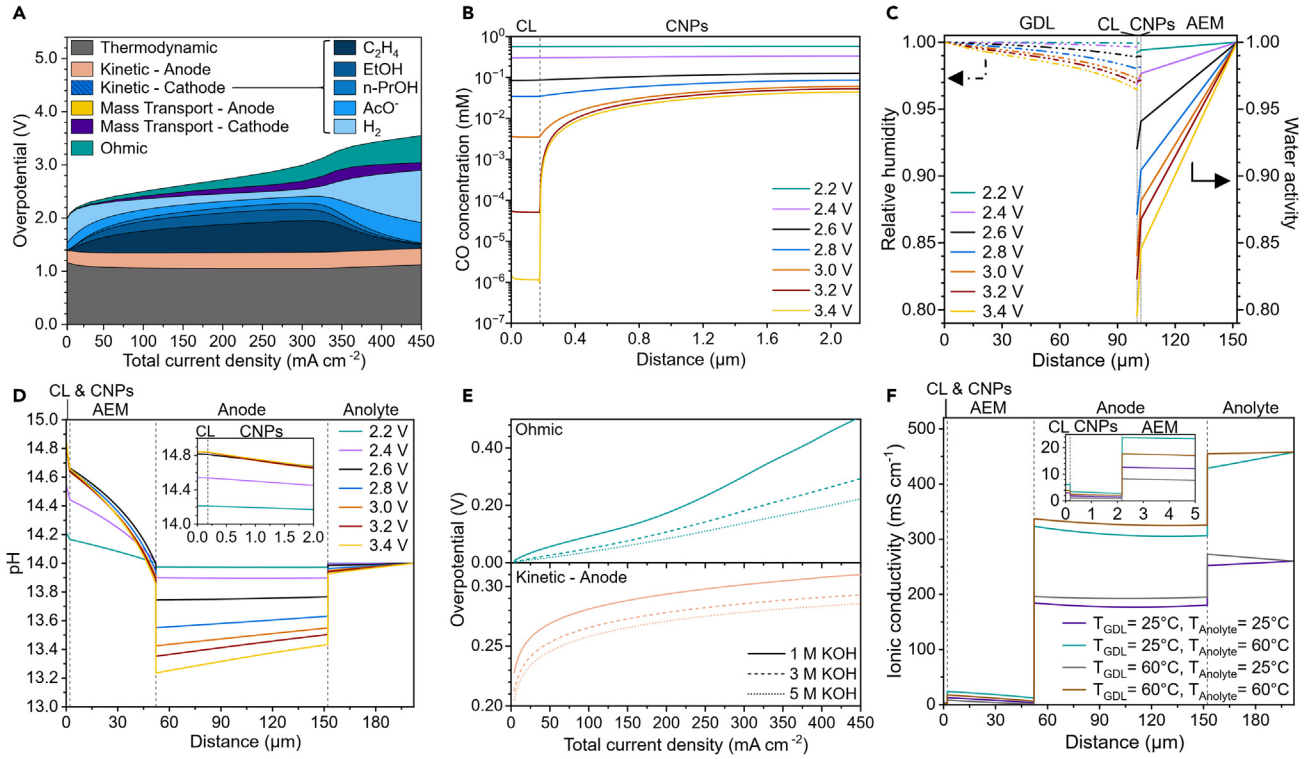

Figure 3. Characteristics of the CO reduction reaction (CORR) in membrane electrode assembly (MEA) electrolyzers

(A) Voltage breakdown analysis of a CORR MEA electrolyzer operating at base case metrics (Table S3). The cathode (i.e., the catalyst layer [CL] and the carbon nanoparticles layer [CNPs]) kinetic overpotential is the summation of each indicated product contribution. The anodic mass transport is minimal (<0.01 V), hence not visible.

(B) CO concentration in the CL and the CNPs at different operating full-cell potentials.

(C) Relative humidity and water activity in the gas diffusion layer (GDL), CL, CNPs, and the anion exchange membrane (AEM).

(D) pH profile in the MEA electrolyzer. The inset shows a larger cross-section of the CL and CNPs.

(E) The ohmic and anodic kinetic overpotentials at variable KOH concentrations.

(F) Ionic conductivity in the MEA electrolyzer as different temperatures are applied to the GDL inlet and/or the anolyte inlet at a full-cell potential of 2.6 V. The inset shows an enlarged view of the CL, CNPs, and AEM.

consumes a tremendous 1.02 V and C_2H_4 consumes a mere 0.05 V). Hence, developing catalysts that selectively utilize electricity to produce value-added products is critical, especially at high current densities.[23,50,51] The anode mass transport overpotential is negligible due to the abundance of OH^- in the anolyte, while the cathode mass transport overpotential increases as the aqueous CO concentration is depleted in the CL (Figure 3B). The water activity in the CL (Figure 3C) also decreases as more water is consumed for CORR and HER, contributing to increased mass transport limitations. The relative humidity (RH) in the gas phase is observed to decrease with higher applied potential as more water is transferred from the gas phase to the reacting liquid phase. However, the RH remains above 95% even at high current densities (Figure 3C), suggesting that the water activity is not limited by RH in this system. The cathode mass transport overpotential reaches a maximum of 0.21 V at ~350 mA cm^{-2}. At higher current densities, this overpotential starts decreasing due to a shift in selectivity from C_{2+} products to H_2 (Figure S10). As for ohmic overpotential, it increases linearly from 0.01 to 0.52 V (Figure 3A). Although ionic conductivity can be enhanced with increasing ion concentration, it peaks as the concentration of K^+ approaches its steric limit in the CL (Figure S11). Conversely, the continuously decreasing water activity in the CL, CNPs, and AEM (Figure 3C) overtakes the increment in ionic conductivity, causing the observed ohmic losses. The

Please cite this article in press as: Alkayyali et al., Pathways to reduce the energy cost of carbon monoxide electroreduction to ethylene, Joule (2024), https://doi.org/10.1016/j.joule.2024.02.014

pH in the CL also reaches a plateau due to the steric limit of OH^- ions, but pH in the anode decreases due to the acidic OER (Figure 3D; Equation 7). Overall, pH remains between 14.2 and 14.8 in the CL, resulting in a highly alkaline environment that is favorable for C_{2+} production while remaining carbonate-free. By understanding how voltage is distributed and utilized in a CORR electrolyzer, the performance of these electrolyzers can be improved via more targeted approaches.

Operating at high anolyte concentrations is an established approach to improve performance in CORR.[13,19,52,53] By modeling the CORR MEA operation with 1, 3, and 5 M KOH, we find that this performance improvement is mainly due to the reduction in ohmic and anode kinetic overpotentials as the KOH concentration is increased (Figure 3E). Ohmic overpotential is lowest when more K^+ is present due to the enhanced ionic conductivity (Figure S12). A higher KOH concentration also decreases the anode kinetic overpotential to a range of 0.21–0.29 V due to faster reaction kinetics.[44]

Another approach to enhance catalytic and system performance is to increase the operating temperature.[18] We computationally test the CORR MEA when temperature is uniformly applied to both the GDL and the anolyte inlets and when a thermal gradient is applied (Figure S13). In our model, operating the whole cell at an elevated temperature (e.g., 60°C) did not offer the largest improvements in performance at the desired low applied full-cell potentials (Figure S14). Prior research and modeling of proton exchange membrane fuel cells showed thermal gradients across the cell,[54] which can become more significant when a coolant is applied to either side of the cell.[55,56] Despite achieving the highest K^+ concentration due to fast diffusion and electromigration when only the GDL is operated at a higher temperature (Figure S15), the high temperature in the cathode region (GDL, CL, and CNPs) increases evaporation, resulting in low water content (Figure S16). A similar trend in water content is observed when both the GDL and anolyte inlets are at an elevated temperature. On the contrary, elevating the temperature of the anolyte while maintaining the cathode at a lower temperature—perhaps through a separate cooling mechanism[57,58]—facilitates a moderate temperature increment in the cathode CL (which enhances C_2H_4 catalysis) while maintaining a high water content (Figure S16). Thus, the highest ionic conductivity in the CL, CNPs, and AEM is achieved when only the anolyte is heated (Figure 3F). The use of a thermally insulative material, such PTFE, as the GDL can create a thermal gradient across the GDL (Figure S13) and enable a local temperature increase in the CL.[59] At base case (i.e., operating the whole cell at room temperature with a PTFE GDL), temperature change in the CL due to Joule heating is observed to be ~1.3°C at 424 mA cm^{-2} (Figure S17). However, if the GDL is made of a heat-conducting material, such as carbon paper, then no temperature change is observed in the CL (Figure S18). With a heat-conducting GDL, operating at room temperature or applying heat to only the anolyte inlet are the best identified modes of operation (Figure S18).

Improving CO-to-C_2H_4 conversion

We first conduct a sensitivity analysis of all model parameters to identify the ones that are most influential with respect to C_2H_4 EE. The cell parameters are individually varied by ±50% (unless otherwise noted) from their base case values (Table S3). The parameters that influence the C_2H_4 EE by > ±5% are shown in Figure 4A, while those of little-to-no influence are shown in Figure S19. The sensitivity analysis reveals that cathode kinetics, namely the C_2H_4 transfer coefficient, activation energy, and exchange current density, are key to increasing the C_2H_4 FE at low full-cell potentials (Figure S20). These parameters are correlated with higher catalyst activity and

Please cite this article in press as: Alkayyali et al., Pathways to reduce the energy cost of carbon monoxide electroreduction to ethylene, Joule (2024), https://doi.org/10.1016/j.joule.2024.02.014

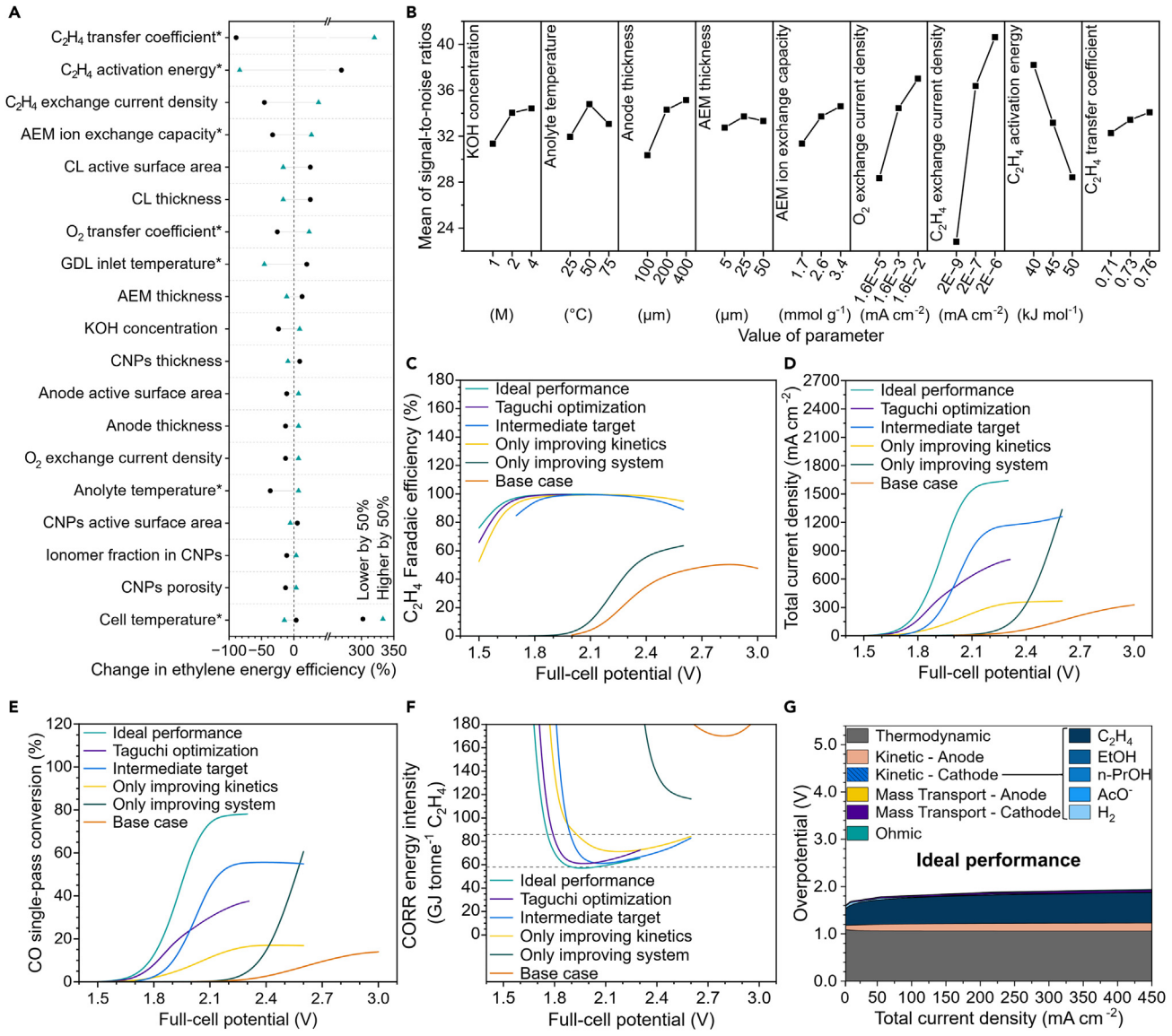

Figure 4. Searching the parameter space that leads to low-energy CO-to-ethylene electroproduction

(A) Tornado plot of the sensitivity results of the parameters showing > ±5% change in ethylene energy efficiency, as each parameter is individually changed by ±50% from its base case value. Asterisks indicate that the parameter is changed by a value other than ±50% (see Table S3).

(B) Taguchi method results for select parameters.

(C–F) Ethylene Faradaic efficiency, total current density, CO single-pass conversion, and CO reduction reaction (CORR) energy intensity for various scenarios (see Table S5). The top dashed line in (F) indicates the intermediate target limit of 86 GJ tonne^{-1} C_2H_4, while the bottom dashed line indicates the ultra-low-energy-target of 58 GJ tonne^{-1} C_2H_4 for the CORR step.

(G) Voltage breakdown analysis of a CORR MEA electrolyzer operating at ideal performance (Table S5). The cathode kinetic overpotential is the summation of each indicated product contribution. No CNPs were considered in (B)–(G).

selectivity.[60] A decreased CL active specific surface area or a decreased CL thickness enhances the selectivity toward C_2H_4, ethanol, and propanol due to the favorable increased cathode kinetic overpotential at these conditions, albeit resulting in lower total current densities (Figure S21).[37] We also investigate the effects of applying a CNPs layer on the CL. We find that a lower active specific surface area of CNPs or a decreased CNPs layer thickness on the CL slightly promotes C_2H_4 formation. When CNPs are used, they contribute to approximately 10%–14% of the produced

Please cite this article in press as: Alkayyali et al., Pathways to reduce the energy cost of carbon monoxide electroreduction to ethylene, Joule (2024), https://doi.org/10.1016/j.joule.2024.02.014

H_2 FE. Without CNPs, the C_2H_4 FE improves by ~2% and the system achieves a higher total current density (Figure S22). A lower ionomer fraction in the CNPs layer decreases ionic conductivity, resulting in HER and a lower total current density, while a higher ionomer fraction does not enhance C_2H_4 formation (Figure S23). The membrane and ionomer ion exchange capacity (IEC) directly affect the ionic conductivity, resulting in higher C_2H_4 production as IEC increases (Figure S24). Thinning the AEM improves both the C_2H_4 FE and total current density while lowering ohmic overpotential (Figure S25). Increasing the anode thickness and kinetics (i.e., O_2 transfer coefficient and exchange current density) helps support the MEA to achieve higher total current densities at the same applied full-cell potentials, with minimal effect on C_2H_4 FE (Figure S26).

With the influence of each cell parameter on CORR MEA performance identified, we investigate the multi-factor effects that determine the set of conditions that could enable ultra-low-energy-intensity C_2H_4. To narrow down the search space, we select the cell parameters that would be most achievable experimentally, that greatly influence EE, and that could be tuned without undermining MEA mechanical integrity and stability. We also opt out of using a CNPs layer on the CL to minimize HER and ohmic losses. However, in this case, a carbon-based GDL that is treated for hydrophobicity is experimentally preferred over pure PTFE due to electrical conductivity limitations in the latter. Alternatively, if carbon paper was used as the GDL, the CL can be equipped with hydrophobicity-enhancing features[22,61,62] and operated at more positive full-cell potentials to prevent flooding.[63]

The selected parameters for multi-factor optimization are anolyte concentration and temperature, anode and AEM thickness, AEM IEC, O_2 and C_2H_4 exchange current density, and C_2H_4 activation energy and transfer coefficient. Running all combinations at three distinct values of each parameter would require ~20,000 simulations. To decrease the cost of multi-factor optimization, we apply the Taguchi design of experiments method[64,65] and create an L27 orthogonal array (Table S4). The parameter values in this array are chosen after running the Taguchi method multiple times at a full-cell potential of 2.0 V and noting the highest simultaneous achievement of total current density (which also contributes to CO SPC) and C_2H_4 FE, resulting in requiring the expansion of the $\pm$50% range used in the sensitivity analysis for some of the parameters. The total current density and C_2H_4 FE resulting from each row of the array are then analyzed using the Taguchi method with larger-the-better criteria (Note S6). By selecting the value of each parameter that results in the highest mean of signal-to-noise ratio (Figure 4B), optimized performance can be anticipated. A confirmation simulation is performed using these parameters (Table S5), and the results show significant improvement in performance over the base case parameters (Figures 4C–4E). The Taguchi optimization result estimates a minimum of 60.6 GJ tonne^{-1} C_2H_4 for the CORR MEA (Figure 4F) at 1.9 V full-cell potential, 375 mA cm^{-2}, 99.5% C_2H_4 FE, and 18% CO SPC, rendering C_2H_4 electroproduction through the cascade system at 83 GJ tonne^{-1} C_2H_4 in overall energy intensity (assuming that the CO is provided at an energy intensity of 22 GJ tonne^{-1} C_2H_4). We explore additionally using a KOH concentration of 1 M, an AEM thickness of 5 μm, and applying 75°C to the anolyte inlet (for reference, 4 M, 25 μm, and 50°C, respectively, were used in the Taguchi optimization; Table S5). With these parameters, the model predicts performance of 56.9 GJ tonne^{-1} C_2H_4 for the CORR MEA at 1.9 V full-cell potential, 643 mA cm^{-2}, 99.7% C_2H_4 FE, and 30.8% CO SPC (Figures 4C–4F). Other ultra-low-energy scenarios are listed in Table S6. Analyzing the voltage breakdown in the ideal performance scenario shows the following improvements compared with the base case: 47%–64% in anode kinetic overpotential,

Please cite this article in press as: Alkayyali et al., Pathways to reduce the energy cost of carbon monoxide electroreduction to ethylene, Joule (2024), https://doi.org/10.1016/j.joule.2024.02.014

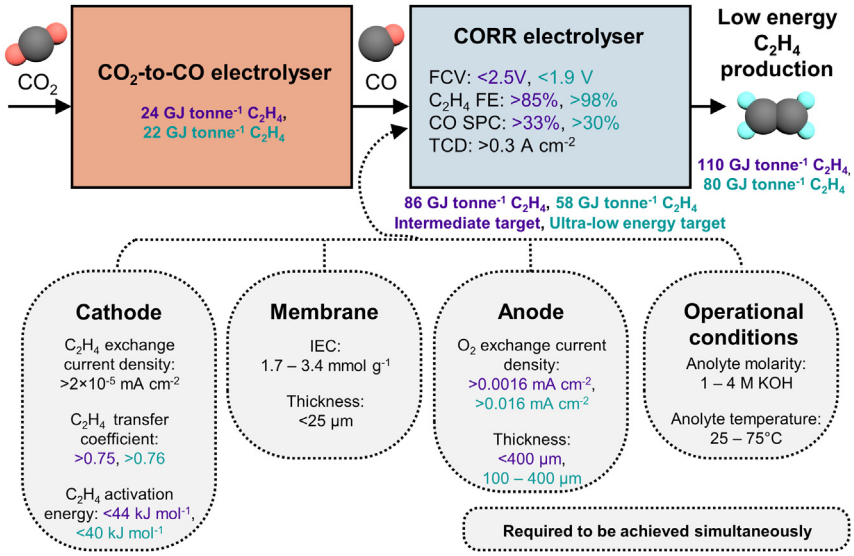

Figure 5. Pathways to low-energy-intensity ethylene electroproduction through the cascade system

A schematic indicating the recommended metrics for the CO reduction reaction (CORR) membrane electrode assembly electrolyzer within a cascade system. A CO_2-to-CO electrolyzer is estimated to require 24 and 22 GJ tonne^{-1} C_2H_4 in the intermediate target and ultra-low-energy-target scenarios, respectively. The CORR electrolyzer energy demand could be as low as 58 GJ tonne^{-1} C_2H_4 once the indicated metrics are achieved. The conclusions arrived at through the model developed in this work are summarized here as recommended ranges of each parameter that is observed to greatly influence the electrolyzer performance. These parameter values are required to be simultaneously achieved in the CORR electrolyzer to reach the indicated energy intensity values. Values in purple correspond to the overall cascade system intermediate target scenario of 110 GJ tonne^{-1} C_2H_4, values in teal correspond to the overall cascade system ultra-low-energy-target scenario of 80 GJ tonne^{-1} C_2H_4, while values in black correspond to both scenarios.

35%–58% in cathode kinetic overpotential, 84% in cathode mass transport overpotential, and 97% in ohmic overpotential at 5–450 mA cm^{-2} (Figure 4G vs. Figure 3A). Such improvements in reducing overpotentials have been previously achieved in water electrolyzers,[66] motivating the rigorous development needed in CORR electrolyzers. The ideal performance scenario is achieved through major improvements (Table S5) to the cathode catalyst, employing a more active anode catalyst, using a thinner and more conductive AEM, and improving the overall operating conditions of the cell. Perhaps the most pressing target, and the most difficult, is for cathode catalyst development to be highly active and selective for C_2H_4 production at low applied full-cell potentials. We discuss suggestions for achieving these targets in more detail in the next section.

We also investigate independently optimizing either the kinetic parameters or the system parameters. We find both optimizations essential; without optimizing kinetic and system parameters together, ultra-low-energy C_2H_4 electroproduction from a CORR MEA is not possible due to insufficient total current density (and hence, CO SPC) or C_2H_4 FE (Figures 4C–4F). Therefore, the simultaneous development of catalyst materials, system components, and operational conditions is required.

Next steps toward low-energy CORR

The CO_2-to-CO and CORR MEA performance metrics for low-energy C_2H_4 electroproduction are outlined in Figure 5. To achieve this performance, the CORR MEA

Please cite this article in press as: Alkayyali et al., Pathways to reduce the energy cost of carbon monoxide electroreduction to ethylene, Joule (2024), https://doi.org/10.1016/j.joule.2024.02.014

must be simultaneously advanced in terms of cathode kinetics (i.e., C_2H_4 activation energy, transfer coefficient, and exchange current density), AEM IEC and thickness, anode kinetics (i.e., O_2 exchange current density), anode thickness, and operational conditions (i.e., KOH concentration and cell temperature). This level of performance exceeds the best results to date, motivating further research into catalysts that achieve high selectivity of CO to C_2H_4 within the MEA.

The past decade saw rapid development in studying and identifying the C_2H_4 pathway in CO_2RR, aided by advancements in characterization methods (such as Raman spectroscopy, X-ray absorption spectroscopy, infrared spectroscopy, isotope labeling, etc.), computational modeling (through density functional theory and molecular dynamics), and system improvement (e.g., pH effect, cation effect, membrane, flow rate, temperature, etc.).[35,67–73] Such research enabled the designing of more efficient and selective CO_2RR catalysts, with performance increasing tremendously from <10% to >87% in C_2H_4 FE[74] or from <10 mA cm^{-2} to >1 A cm^{-2} in C_2H_4 partial current density,[75] although simultaneous achievement of high C_2H_4 FE and partial current density is still challenging. In CORR, future cathode catalysts can similarly be designed and optimized by improving surface morphology,[76–78] doping with a secondary element,[79,80] improving charge transfer kinetics,[81] enhancing the electrochemically active surface area,[14,15,82,83] and/or by other methods.[12,84,85] Through such developments, lower full-cell potentials would also be attainable due to the decreased cathode kinetic overpotential. Many of the system requirements for the 110 GJ $tonne^{-1}$ C_2H_4 target are similar to those of the ultra-low-energy 80 GJ $tonne^{-1}$ C_2H_4 reference value, with the key differences being in the catalyst selectivity and full-cell potential thresholds. In parallel, thin membrane layers (<25 μm) with improved ionic exchange capacity (1.7–3.4 mmol g^{-1}) are needed to achieve the current density required. Such IECs have mostly been achieved,[86,87] albeit higher IECs increase water uptake.[87] Designing AEMs with low-to-moderate water uptake is crucial for maintaining the desired ionic conductivity while preventing flooding at the cathode CL.[88] The AEM must also withstand the mechanical stress in the cell, a challenge that is acute when employing low AEM thicknesses and when cells are scaled up. Thin, non-commercial membranes (<10 μm) have been applied in CO_2RR[89] (via a cation exchange membrane [CEM]) and fuel cells[90,91] (via AEM and CEM), but thin AEM deployment in CORR with low water crossover and long stability is yet to be explored. Another target for future CORR research is to improve the anode activity, which is critical to decreasing the anode kinetic overpotential and, thereby, lowering the operational full-cell potential. Thicker anodes (>100 μm) can also enable higher total current densities. The electrolyzer capital costs can be decreased if nonprecious materials are used in constructing the anode. Ni or Ni alloy anodes have been shown to decrease the CORR full-cell potential by >0.2 V compared with IrO_2 anodes.[87] Ni-based anodes are also better suited for alkaline environments,[4,62,92] which are inherent in CORR electrolyzers. Optimizing the KOH concentration (1–4 M) and the cell/anolyte temperature (25°C–75°C) could further promote the total current density and C_2H_4 selectivity. Ranges for the above recommended parameters that could permit the ultra-low CORR energy intensity of $\leq$58 GJ $tonne^{-1}$ C_2H_4 are shown in Table S6. Other parameters (e.g., CL thickness, CL porosity, and GDL material and hydrophobicity) could offer additional enhancements to the CORR MEA performance,[14,15] but the above recommended parameters are found to be the most influential in decreasing the operational energy of the CORR MEA. In this work, a higher total current density was required to increase the CO SPC (in combination with a high C_2H_4 FE). Operating at a higher current density also enables a significant decrement in electrolyzer capital costs, but will require advances

Please cite this article in press as: Alkayyali et al., Pathways to reduce the energy cost of carbon monoxide electroreduction to ethylene, Joule (2024), https://doi.org/10.1016/j.joule.2024.02.014

in sustained stable operation.[93] Other methods of promoting the CO SPC could also be implemented, such as decreasing the inlet gas flow rate or using materials that enhance CO adsorption and availability near the catalyst surface.[94] Lastly, we note that two-step cascade systems will require further progress and scalability—and reliability of operation under intermittent conditions—of CO_2-to-CO electrolyzers, in addition to progress in the CORR electrolyzer that is the principal focus of this work.

Conclusions

We developed a model of the electrochemical CORR toward C_{2+} products in a MEA electrolyzer. We validated and applied this model to screen the effects of cell parameters on CORR performance and to outline specific improvements that are required to produce C_2H_4 at a low energy intensity through a carbonate-free cascade system. To achieve low energy intensity, C_2H_4 electroproduction in the CORR step requires significant and simultaneous advances in catalysts and system components. The C_2H_4 catalyst activity and selectivity must be greatly improved. The AEM thickness will need to be decreased while increasing the IEC, reducing the water uptake, and remaining mechanically robust. More active anodes with nonprecious materials are necessary for the CORR MEA. We also show that system operating conditions, such as KOH concentration and temperature, can further reduce the CORR energy intensity. Through optimization of key parameters, the model predicts a minimum energy intensity for the CORR step of 56.9 GJ tonne^{-1} C_2H_4, with a noticeable reduction in overpotentials compared with the unoptimized system, yielding 79.3 GJ tonne^{-1} C_2H_4 in overall energy intensity if combined with a 22 GJ tonne^{-1} C_2H_4 CO_2-to-CO electrolyzer. Achieving this level of performance will be challenging. This work motivates targeted material development and experimental directions toward the goal of low-energy-intensity electro-produced C_2H_4.

EXPERIMENTAL PROCEDURES

Resource availability

Lead contact

Further information and requests for resources should be directed to and will be fulfilled by the lead contact, David Sinton (sinton@mie.utoronto.ca).

Materials availability

This study did not generate new unique materials.

Data and code availability

The data presented in this work are available from the corresponding author upon reasonable request. The model presented in this work is available as a MATLAB code on Zenodo: https://doi.org/10.5281/zenodo.10633054.

Numerical method

The model is built and solved using COMSOL Multiphysics v6.0. A fully coupled approach is used in a stationary solver. The governing equations are solved using a direct MUMPS solver, with an automatic Newton nonlinear method and a relative tolerance of 0.001 and 8,818 degrees of freedom (with 60 internal degrees of freedom). The solver comprises sequential steps of increasing complexity to allow for solution convergence, with a final step simultaneously solving all multi-physics. The modeling domains are meshed using symmetric edge mesh distribution with a linear growth rate and a total of 992 elements. The number of elements in each domain (Table S7) is chosen based on a mesh independence test (Figure S27).

Please cite this article in press as: Alkayyali et al., Pathways to reduce the energy cost of carbon monoxide electroreduction to ethylene, Joule (2024), https://doi.org/10.1016/j.joule.2024.02.014

Aqueous species transport

The mass balance of aqueous species i (i.e., K^+, OH^-, H^+, $CO_{(aq)}$) is modeled as[37]

$$\nabla \cdot N_i + u_l \cdot \nabla c_i = R_{PT} + \varepsilon_{p,d} R_{B,i} + \sum_m R_{CT,i,m} \quad \text{(Equation 9)}$$

where N_i is the molar flux of species i, u_l is the liquid-phase velocity, c_i is the local concentration of species i, R_{PT} is the source term due to phase transport, $\varepsilon_{p,d}$ is the volume fraction of phase p (i.e., g for gas, l for liquid, I for ionomer, and s for solid) in domain d (i.e., the GDL, CL, CNPs, AEM, anode, or anolyte), $R_{B,i}$ is the source term due to bulk homogeneous reactions (i.e., water dissociation), and $R_{CT,i,m}$ is the source term due to a charge transfer reaction m (i.e., ethylene, ethanol, propanol, acetate, hydrogen, or oxygen evolution). The Nernst-Planck equation is used to describe the molar flux through diffusion and electromigration as[37]

$$N_i = -D_{i,p}^{eff} \nabla c_i - \frac{z_i D_{i,p}^{eff} F c_i \nabla \varphi_l}{RT} \quad \text{(Equation 10)}$$

where $D_{i,p}^{eff}$ is the effective diffusion coefficient of species i, z_i is the charge of species i (zero for $CO_{(aq)}$), F is the Faraday constant, φ_l is the electrolyte potential, R is the universal gas constant, and T is the calculated temperature.

The phase transport source term pertains to CO transport from the gas phase to the liquid phase and is defined in either the CL or the CNPs layer as[37–39]

$$R_{PT} = \frac{D_{CO}^{(T)}}{\delta_{TF,d}\left(1 - \sqrt{1 - S_{l,d}}\right)} a_{v,d}^{active}\left(c_{CO_{(aq)}}^{max} - c_{CO_{(aq)}}\right) \quad \text{(Equation 11)}$$

where $D_{CO}^{(T)}$ is the diffusion coefficient of CO as a function of temperature (Table S8), $\delta_{TF,d}$ is the thin-film thickness coefficient, $S_{l,d}$ is the liquid-phase saturation, and $a_{v,d}^{active}$ is the active specific surface area, which is related to the intrinsic specific surface area, $a_{v,d}^0$, via[37]

$$a_{v,d}^{active} = a_{v,d}^0 (1 - S_{l,d}) \quad \text{(Equation 12)}$$

The maximum aqueous CO concentration, according to pressure, temperature, and salinity, $c_{CO_{(aq)}}^{max}$, is governed by Henry's law and the Sechenov equation as follows[40]

$$c_{CO_{(aq)}}^{max} = P_{CO_{(g)}} K_{Henry,CO} 10^{-c_{Sechenov,CO}} \quad \text{(Equation 13)}$$

$$K_{Henry,CO} = A_{CO}^{B_{CO}\left(\frac{1}{T} - \frac{1}{298.15\ [K]}\right)} \quad \text{(Equation 14)}$$

$$c_{Sechenov,CO} = \sum_{i,i \neq CO_{(aq)}} c_i \left[\frac{mol}{dm^3}\right] (h_i + h_{G,0} + h_T(T - 298.15\ [K])) \quad \text{(Equation 15)}$$

in which $P_{CO_{(g)}}$ is the CO partial pressure in the gas phase, A_{CO} is a Henry's law constant for CO (9.8×10^{-6} mol m^{-3} Pa^{-1}), B_{CO} is another Henry's law constant (1,300 K), h_i is an ion-dependent Sechenov constant (0.0922 m^3 $kmol^{-1}$ for K^+, 0.0839 m^3 $kmol^{-1}$ for OH^-, and zero for H^+), while $h_{G,0}$ and h_T are gas-dependent Sechenov constants (set to the CO_2 values of -0.0172 m^3 $kmol^{-1}$ and -0.000338 m^3 $kmol^{-1}$ K^{-1}, respectively, due to the lack of relevant data on CO).[95,96]

Bulk homogeneous reactions are defined as[97]

$$R_{B,H^+} = R_{B,OH^-} = k_{w,f} - k_{w,r} c_{H^+} c_{OH^-} \quad \text{(Equation 16)}$$

where k_{wf} and k_{wr} are the forward and backward water dissociation rate constants, 2.4×10^{-5} mol L^{-1} s^{-1} and 2.4×10^{9} L mol^{-1} s^{-1}, respectively.[98]

The charge transfer reaction source term is defined through Faraday's law as[38]

$$R_{CT,i,m} = -\frac{\nu_{i,m} a_{v,d}^{active} i_{v,m}}{n_m F} \quad \text{(Equation 17)}$$

in which $\nu_{i,m}$ is the stochiometric coefficient of species i in charge transfer reaction m, $i_{v,m}$ is the partial current density of the reaction, and n_m is the number of participating electrons in the reaction.

Properties that are denoted as effective, X_d^{eff}, are corrected from their intrinsic values, X_d^0, for tortuosity and porosity in porous domains according to the Bruggeman model,[37,42] such that

$$X_d^{eff} = \varepsilon_{p,d}^{1.5} X_d^0 \quad \text{(Equation 18)}$$

The volume fraction of the target phase in each domain, $\varepsilon_{p,d}$, is corrected from the intrinsic domain porosity, ε_d^0, as per the following relationships[37]:

$$\varepsilon_{s,d} = 1 - \varepsilon_d^0 \quad \text{(Equation 19)}$$

$$\varepsilon_{l,d} = \varepsilon_d^0 f_{l,d} \quad \text{(Equation 20)}$$

$$\varepsilon_{l,d} = \varepsilon_d^0 (1 - f_{l,d}) S_{l,d} \quad \text{(Equation 21)}$$

$$\varepsilon_{g,d} = \varepsilon_d^0 (1 - f_{l,d})(1 - S_{l,d}) \quad \text{(Equation 22)}$$

where $f_{l,d}$ is the ionomer volume fraction.

In the membrane, CL, and CNPs domains, the diffusion of charged species is calculated as[38]

$$D_{i,p}^{eff} = \frac{\varepsilon_w D_i^{(T)}}{x_w (1+\zeta_i)} \quad \text{(Equation 23)}$$

where ε_w is the water volume fraction, defined as

$$\varepsilon_w = \frac{\lambda V_w}{\lambda V_w + V_M} \quad \text{(Equation 24)}$$

The values of the diffusion coefficient as a function of temperature, $D_i^{(T)}$, are listed in Table S8. The water content, λ, is defined by[37,38]

$$\lambda = 30.75 a_w^3 - 41.19 a_w^2 + 21.14 a_w + \frac{1}{5}(T - T_{in}) \quad \text{(Equation 25)}$$

where a_w is the water activity and T_{in} is the temperature at the cathode inlet (25°C). The water molar volume, V_w, is 1.807×10^{-5} m^3 mol^{-1}, while the membrane molar volume, V_M, is defined as

$$V_M = \frac{1}{IEC\ \rho_M} \quad \text{(Equation 26)}$$

where ρ_M is the membrane density (1.4 g cm^{-3}). The water mole fraction, x_w, is defined as

$$x_w = \frac{\lambda}{1+\lambda} \quad \text{(Equation 27)}$$

Please cite this article in press as: Alkayyali et al., Pathways to reduce the energy cost of carbon monoxide electroreduction to ethylene, Joule (2024), https://doi.org/10.1016/j.joule.2024.02.014

The kinetic theory is used to describe the ratio of species-water and species-membrane interactions as follows[38]

$$\zeta_i = \frac{1}{\lambda}\left(\frac{V_M}{V_w}\right)^{2/3}\left(\frac{M_{i,M}}{M_{i,w}}\right)^{1/2} \quad \text{(Equation 28)}$$

where $M_{i,M}$ is defined as

$$M_{i,M} = \left(\frac{1}{M_i}+\frac{1}{M_M}\right)^{-1} \quad \text{(Equation 29)}$$

and $M_{i,w}$ is defined as

$$M_{i,w} = \left(\frac{1}{M_i}+\frac{1}{M_w}\right)^{-1} \quad \text{(Equation 30)}$$

where M_i is the molar mass of species i, M_M is the molar mass of the membrane ($\rho_{AEM} \times V_M$), and M_w is the molar mass of water.

The flux of water in the ionomer and membrane is calculated by[37,99,100]

$$N_w = -D_w^{eff}\nabla c_w - \frac{\xi_d i_l}{F} \quad \text{(Equation 31)}$$

$$\nabla \cdot N_w = 0 \quad \text{(Equation 32)}$$

where D_w^{eff} is the effective diffusion coefficient of water (Table S8), ξ_d is the electro-osmotic drag coefficient of water, and i_l is the electrolyte current density. Water concentration in the ionomer or membrane, c_w, is calculated as[101]

$$c_w = \frac{\rho_w}{\lambda M_w} \quad \text{(Equation 33)}$$

in which ρ_w is the water density (1.0 g cm^{-3}). Water activity is calculated as

$$a_w = \frac{c_w}{c_w^0} \quad \text{(Equation 34)}$$

where the intrinsic water concentration, c_w^0, is calculated from the intrinsic water content, λ^0 (Table S3).

Charge transfer and conservation

A concentration-dependent Butler-Volmer expression is used to calculate the partial current density in the cathode (i.e., CL or CNPs) as[37,38]

$$i_{v,m} = -i_{0,m}^{\dagger}\left(\frac{c_i}{c_{ref}}\right)^{d_{c_i,m}} a_w^{d_{H_2O,m}} \exp\left(-\frac{\alpha_m F \eta_m}{RT}\right) \quad \text{(Equation 35)}$$

while for the anode, the partial current density is defined as

$$i_{v,m} = i_{0,m}^{\dagger}\left(\frac{c_i}{c_{ref}}\right)^{d_{c_i,m}} \exp\left(\frac{\alpha_m F \eta_m}{RT}\right) \quad \text{(Equation 36)}$$

in which $i_{0,m}^{\dagger}$ is the calculated exchange current density, c_{ref} is a reference concentration, $d_{c_i,m}$ is an exponent of the reactant concentration term, $d_{H_2O,m}$ is an exponent of water activity, and α_m is the transfer coefficient. The local $CO_{(aq)}$ and OH^- concentrations, quantified via c_i, influence the rate of formation of carbon-containing products at the cathode and basic OER at the anode, respectively. All cathode reduction reactions are also affected by the available water activity. The electrode potential, η_m, is defined as

$$\eta_m = \varphi_s - \varphi_l - \left(E_{eq,m} - \frac{2.303RT}{F} pH_{local}\right) \quad \text{(Equation 37)}$$

Please cite this article in press as: Alkayyali et al., Pathways to reduce the energy cost of carbon monoxide electroreduction to ethylene, Joule (2024), https://doi.org/10.1016/j.joule.2024.02.014

where φ_s is the electric potential, $E_{eq,m}$ is the equilibrium half-cell potential of reaction m at standard conditions, and pH_{local} is the local calculated pH. All kinetic-related values are listed in Table S9 and are based on initial values from a previous report on CO_2RR with Cu and OER with IrO_2.[37] The Butler-Volmer parameter values have been fitted to experimental results according to the procedure outlined in Note S3.

By way of charge conservation, the electrolyte current density is defined as

$$\nabla \cdot i_l = \varepsilon_{p,d} F \sum_i z_i R_{CT,i,m} + \sum_m i_{v,m} \quad \text{(Equation 38)}$$

and the electrolyte potential is solved by

$$i_l = F \sum_i z_i N_i \quad \text{(Equation 39)}$$

The electric current density is conserved as follows

$$\nabla \cdot i_s = -\varepsilon_{p,d} F \sum_i z_i R_{CT,i,m} - \sum_m i_{v,m} \quad \text{(Equation 40)}$$

and Ohm's law is used to calculate electric potential,

$$i_s = -\sigma_{s,d}^{eff} \nabla \varphi_s \quad \text{(Equation 41)}$$

where $\sigma_{s,d}^{eff}$ is the effective domain electrical conductivity. In the above equations, the volume fraction refers to the electrolyte volume fraction in the ionomer phase or that in the liquid phase if no ionomer is used in the target domain. The electrolyte volume fraction is also assumed to be equal to one in the AEM domain. Electroneutrality is governed by

$$\sum_i z_i c_i = 0 \quad \text{(Equation 42)}$$

Gaseous species transport

The transport of gaseous species j (or k; i.e., CO, $H_2O_{(g)}$, C_2H_4, and H_2) in the porous GDL, CL, and CNPs is solved using a mixture-averaged diffusion model described by[37,38]

$$\nabla \cdot J_j + \rho_g (u_g \cdot \nabla) \omega_j = Q_{j,total} \quad \text{(Equation 43)}$$

where J_j is the mass flux, ρ_g is the gas mixture density, u_g is the gas-phase velocity, ω_j is the mass fraction. The mass flux is defined as

$$J_j = -\rho_g D_{j,MSK}^{eff} \nabla \omega_j - \rho_g \omega_j D_{j,MSK}^{eff} \frac{\nabla M_{mix}}{M_{mix}} \quad \text{(Equation 44)}$$

where ρ_g is calculated assuming an ideal gas at an absolute pressure, P_A, of 1 atm by

$$\rho_g = \frac{P_A M_{mix}}{RT} \quad \text{(Equation 45)}$$

The average molar mass of the mixture is calculated as

$$M_{mix} = \left(\sum_j \frac{\omega_j}{M_j} \right)^{-1} \quad \text{(Equation 46)}$$

where M_j is the molar mass of species j. The effective Maxwell-Stefan-Knudsen diffusion coefficient, $D_{j,MSK}^{eff}$, is defined as

$$D_{j,MSK}^{eff} = \varepsilon_{g,d}^{1.5} D_{j,MSK}^{0} \quad \text{(Equation 47)}$$

Please cite this article in press as: Alkayyali et al., Pathways to reduce the energy cost of carbon monoxide electroreduction to ethylene, Joule (2024), https://doi.org/10.1016/j.joule.2024.02.014

$$D^{0}_{j,MSK} = \left(\frac{1}{D_{j,MS}} + \frac{1}{D_{j,K}}\right)^{-1} \quad \text{(Equation 48)}$$

The Maxwell-Stefan diffusivity, $D_{j,MS}$, is calculated from the binary diffusion coefficient of gaseous species j and k, D_{j-k} (Table S8), and the mole fraction of species k, y_k, as

$$D_{j,MS} = \frac{1 - \omega_j}{\sum_{k \neq j} \frac{y_k}{D_{j-k}}} \quad \text{(Equation 49)}$$

The Knudsen diffusion coefficient, $D_{j,K}$, is based on the kinetic gas theory and is calculated as

$$D_{j,K} = \frac{2}{3} r_{pore,d} \sqrt{\frac{8RT}{\pi M_j}} \quad \text{(Equation 50)}$$

in which $r_{pore,d}$ is the average pore radius in domain d.

The consumption, evolution, evaporation, or condensation of a gaseous species is accounted for as applicable through a source term $Q_{j,total}$, which is specified as

$$Q_{j,total} = -M_j \left(R_{PT} + \frac{a^{active}_{v,d} i_{v,m}}{F} + Q_{EC,w}\right) \quad \text{(Equation 51)}$$

in which $Q_{EC,w}$ is a source term that pertains to water evaporation and condensation (described in the following section).

Gas- and liquid-phase transport

The gas- and liquid-phase pressures are related by capillary pressure, P_c, defined as[102]

$$P_c = P_g - P_l \quad \text{(Equation 52)}$$

where P_g is the gas-phase pressure and P_l is the liquid-phase pressure. Capillary pressure is used to determine the liquid-phase saturation in the cathode porous domains through the saturation curves shown by Weng et al.[37] The liquid saturation in the CL and the CNPs is assumed to be the same. The liquid saturation curves are shifted down by 0.1-unit saturation at all P_c values in the CL and the CNPs and at $P_c > 0$ in the GDL to account for the higher hydrophobicity offered by PTFE compared with carbon paper.[39] Ions are assumed to transport through the calculated wetting layer in the CL when sputtered Cu (i.e., no ionomer) is used. The gas-phase saturation, $S_{g,d}$, is calculated by[102]

$$S_{g,d} = 1 - S_{l,d} \quad \text{(Equation 53)}$$

Darcy's law is used to calculate the pressure and velocity of the gas and liquid phases as

$$u_p = -\frac{\psi^{eff}_{p,d}}{\mu_p} \nabla P_p \quad \text{(Equation 54)}$$

where $\psi^{eff}_{p,d}$ is the effective permeability of each phase in the domain of interest. This property is calculated as follows[39]

$$\psi^{eff}_{p,d} = \psi^{sat}_{p,d} \psi^{r}_{p,d} \quad \text{(Equation 55)}$$

The saturated permeability, $\psi^{sat}_{p,d}$, is calculated as

$$\psi^{sat}_{p,d} = \psi^{0}_{d} \frac{\varepsilon^{3}_{p,d}}{(1 - \varepsilon_{p,d})^{2}} \quad \text{(Equation 56)}$$

Please cite this article in press as: Alkayyali et al., Pathways to reduce the energy cost of carbon monoxide electroreduction to ethylene, Joule (2024), https://doi.org/10.1016/j.joule.2024.02.014

where ψ_d^0 is the intrinsic permeability. The relative permeability, $\psi_{p,d}^r$, is calculated as

$$\psi_{p,d}^r = (1 - S_{p,d})^3 \quad \text{(Equation 57)}$$

The viscosity, μ_p, is considered to be that of CO in the gas phase (1.74×10^{-2} mPa·s) and that of water in the liquid phase (1.0016 mPa·s).

The following equation is used to describe species transport between the gas and liquid phases,[37]

$$\nabla \cdot (\rho_p u_p) = Q_{p,total} \quad \text{(Equation 58)}$$

where $Q_{p,total}$ is a source term describing the summation of each phase transport phenomenon occurring in the phase of interest. In the liquid phase, $Q_{p,total}$ is defined as

$$Q_{l,total} = Q_{EC,w} + M_w \sum_m \frac{\nu_{w,m} a_{v,d}^{active} i_{v,m}}{n_m F} - Q_{l,w} + Q_{RH,w} \quad \text{(Equation 59)}$$

and in the gas phase, it is defined as

$$Q_{g,total} = -Q_{EC,w} - M_j \sum_{m,m = C_2H_4 \text{ or } H_2} \frac{a_{v,d}^{active} i_{v,m}}{F} - M_{CO} R_{PT} - Q_{RH,w} \quad \text{(Equation 60)}$$

Water evaporation and condensation, $Q_{EC,w}$, is described by

$$Q_{EC,w} = M_w a_{v,d}^{active} k_{MT,g} \frac{(y_w P_g - P_{vap})}{1\ [atm]} \quad \text{(Equation 61)}$$

where $k_{MT,g}$ is a water vapor mass transport coefficient (0.06 mol m^{-2} s^{-1})[37] and P_{vap} describes the water vapor pressure at the calculated temperature as[38]

$$P_{vap} = 1\ [mmHg] \times 10^{8.07 - \frac{1,730.63}{T\ [K] - 39.724}} \quad \text{(Equation 62)}$$

The source term of water from the ionomer to the liquid phase, $Q_{l,w}$, is defined as

$$Q_{l,w} = M_w a_{v,d}^{active} k_{MT,l} \left(\frac{1}{RT} (P_l - a_w \times 1\ [atm]) \right) \quad \text{(Equation 63)}$$

where $k_{MT,l}$ is a water mass transport coefficient (10^4 m s^{-1}).[37] The RH, is ensured to be $\leq$100% through a Heaviside step function, $H_0(x)$, which is activated once the RH exceeds 100%. Therefore, $Q_{RH,w}$ is defined as

$$Q_{RH,w} = M_w k_{MT,RH} (RH - 100\%) [H_0(RH > 100\%)] \quad \text{(Equation 64)}$$

where $k_{MT,RH}$ is a mass transport coefficient (10^7 mol m^{-3} s^{-1})[37] and RH is defined as

$$RH = \frac{y_w P_g \times 100\%}{P_{vap}} \quad \text{(Equation 65)}$$

Heat transfer

Heat flux through the system, q, is governed by[37,38]

$$q = -k_{T,p,d}^{\dagger} \nabla T \quad \text{(Equation 66)}$$

$$\nabla \cdot q = \Omega_{CT} + \Omega_B + \Omega_{EC} + \Omega_J \quad \text{(Equation 67)}$$

where $k_{T,p,d}^{\dagger}$ is the calculated thermal conductivity in porous domain d and is defined as

$$k_{T,p,d}^{\dagger} = (1 - \varepsilon_{s,d}) k_{T,fluid,d} + \varepsilon_{s,d} k_{T,s,d} \quad \text{(Equation 68)}$$

Please cite this article in press as: Alkayyali et al., Pathways to reduce the energy cost of carbon monoxide electroreduction to ethylene, Joule (2024), https://doi.org/10.1016/j.joule.2024.02.014

where $k_{T,fluid,d}$ and $k_{T,s,d}$ are the fluid- and solid-phase thermal conductivity, respectively (Table S3). Other heat transfer properties are listed in Table S10.

The heat generated through charge transfer reactions is expressed as[37]

$$\Omega_{CT} = \sum_{m}\left(a_{v,d}^{active} i_{v,m} \eta_m + a_{v,d}^{active} i_{v,m} \Pi_m\right) \quad \text{(Equation 69)}$$

in which Π_m is the Peltier coefficient for each reaction m (Table S11). Heat associated with the water dissociation reaction is expressed as

$$\Omega_B = \Delta H_B R_{B,H^+} \quad \text{(Equation 70)}$$

where ΔH_B is the water dissociation enthalpy change (55.84 kJ mol^{-1}).[38] Water evaporation and condensation in the cathode domains results in heat generation/consumption, which is defined as[37]

$$\Omega_{EC} = -\left(H_{vap}^{(T)} - H_{vap}^{(T_{in})}\right) k_{MT,RH}(100\% - RH)[H_0(RH>100\%)] \quad \text{(Equation 71)}$$

where $H_{vap}^{(T)}$ and $H_{vap}^{(T_{in})}$ is the water heat of vaporization (Table S12) at the calculated temperature, T, and at the starting temperature, T_{in}, respectively. Joule heating is defined as[37]

$$\Omega_J = \frac{i_s^2}{\sigma_{s,d}^{eff}} + \frac{i_l^2}{\sigma_{l,d}^{eff}} \quad \text{(Equation 72)}$$

where $\sigma_{l,d}^{eff}$ is the effective electrolyte conductivity, which is internally calculated by COMSOL according to the following equation

$$\sigma_{l,d}^{eff} = \sum_{i,i\neq CO_{(aq)}} \frac{c_i D_{i,p}^{eff} (z_i F)^2}{RT} \quad \text{(Equation 73)}$$

Boundary conditions and model considerations

The boundary conditions used in the model are illustrated in Figure 2. Briefly, the mass fraction of gaseous species at the GDL left-hand side inlet boundary is defined in terms of the mole fraction, such that

$$\omega_j = \omega_{j,in} = \frac{y_{j,in} M_j}{M_n} \quad \text{(Equation 74)}$$

where $y_{j,in}$ is $1 - \frac{P_{vap}}{P_g}$ for CO, $\frac{P_{vap}}{P_g}$ for $H_2O_{(g)}$, and zero for ethylene. The liquid-phase pressure at this boundary is defined as the difference between the gas-phase pressure and the capillary pressure obtained at the GDL inlet saturation, $S_{l,GDL}$. The gas-phase pressure is defined as the inlet gas pressure (1 atm). Temperature is defined as the inlet gas temperature at the base case (25°C). The mass constraint is assumed from ω_{j,H_2}.

At the boundary between the GDL and CL, the electric potential is defined as the applied full-cell potential (negative; however, all data plots in this work report the absolute value of full-cell potential for convenience). No CO flux is assumed at this boundary. Because the Nernst-Planck equations assume dilute solution theory and result in unphysical ion concentrations at charged surfaces,[97] we include a concentration boundary condition at the CL left-hand side boundary to limit the concentration of K^+ and OH^- to their estimated steric limit as follows

$$c_{OH^-} = \frac{1}{N_A a_{K^+}^3} \quad \text{(Equation 75)}$$

Please cite this article in press as: Alkayyali et al., Pathways to reduce the energy cost of carbon monoxide electroreduction to ethylene, Joule (2024), https://doi.org/10.1016/j.joule.2024.02.014

in which N_A is the Avogadro's constant and a_{K^+} is the effective size of the solvated K^+ ion (0.662×10^{-9} m).[97] This boundary condition is activated only when $c_{OH^-} \geq c_{K^+}^{max}$, which is ~6.9 M. Because $c_{OH^-}^{max}$ is ~7.7 M, the steric limit is assumed to be that of K^+. Not accounting for this boundary condition results in extremely high ion concentrations in the CL and CNPs layer (Figure S28), a consequent depletion of the calculated CO concentration, and a suppression of all CORR reactions. Accounting for all effects of the electrical double layer (<0.1 μm in thickness) is not possible in the current model due to the large scale of the modeled domains. However, the obtained ion concentrations using the approach described herein are in agreement with published literature that explicitly models the electrical double layer.[97]

At the boundary between the CNPs and the AEM, no flux is assumed for $CO_{(aq)}$ and the gaseous species. No gas or liquid flow is also assumed at this boundary. A Dirichlet boundary condition is applied at the boundary between the AEM and anode to specify the water concentration as c_w^0. The electric potential is set to ground at the boundary between the anode and anolyte. The anolyte right-hand side is assumed to be electrically insulated. The concentration of ions is specified to resemble the inlet anolyte concentration of 1 M KOH at the base case (i.e., $c_{OH^-,in}$ is 1,000 mol m^{-3} and $c_{H^+,in}$ is 1×10^{-11} mol m^{-3}). Electroneutrality is assumed from c_{K^+}. Temperature is defined at this boundary as the inlet anolyte temperature at the base case (25°C).

The phase transport of gaseous CORR products (i.e., ethylene and hydrogen) from the liquid phase to the gas phase is assumed to occur quickly due to the low solubility of these gases in water.[103] Due to the limited available information on the mass transport of liquid CORR products (i.e., ethanol, propanol, and acetate) in the ionomer and membrane, these products are assumed to leave the system rapidly.[37] The GDL is assumed to inherently have a microporous layer, which was not explicitly defined in the described model. The cross-sectional area of the cell is assumed to be 5 cm^2. The initial values of certain parameters are specified in Table S13.

SUPPLEMENTAL INFORMATION

Supplemental information can be found online at https://doi.org/10.1016/j.joule.2024.02.014.

ACKNOWLEDGMENTS

The authors acknowledge funding for this work from the Government of Canada's New Frontiers in Research Fund (NFRF), CANSTOREnergy project NFRFT-2022-00197, the Natural Sciences and Engineering Research Council of Canada (NSERC), and the Canada Research Chairs Program. The authors acknowledge CMC Microsystems for the provision of products and services that facilitated this research, including COMSOL Multiphysics. T.A. acknowledges NSERC, Hatch, and the University of Toronto for their support through graduate scholarships and fellowships.

AUTHOR CONTRIBUTIONS

D.S. and E.H.S. supervised the project. T.A. conceived the idea, designed the model, carried out all computations, and prepared the manuscript. M.Z. helped with model design. A.O. performed all experiments and assisted in energy analyses. F.A. performed the voltage diagnostic experiment. A.B., R.D., J.P.E., F.L., A.S.Z., and M.F. contributed to valuable discussions on the work. All authors contributed to editing the manuscript.

DECLARATION OF INTERESTS

The authors declare no competing interests.

Received: October 27, 2023
Revised: January 13, 2024
Accepted: February 16, 2024
Published: March 7, 2024

REFERENCES

1. Zhu, Q. (2019). Developments on CO_2-utilization technologies. Clean Energy *3*, 85–100.
2. Rafiee, A., Rajab Khalilpour, K., Milani, D., and Panahi, M. (2018). Trends in CO_2 conversion and utilization: A review from process systems perspective. J. Environ. Chem. Eng. *6*, 5771–5794.
3. Sisler, J., Khan, S., Ip, A.H., Schreiber, M.W., Jaffer, S.A., Bobicki, E.R., Dinh, C.-T., and Sargent, E.H. (2021). Ethylene Electrosynthesis: A Comparative Techno-economic Analysis of Alkaline vs Membrane Electrode Assembly vs CO_2–CO– C_2H_4 Tandems. ACS Energy Lett. *6*, 997–1002.
4. Vass, Á., Kormányos, A., Kószo, Z., Endrődi, B., and Janáky, C. (2022). Anode Catalysts in CO_2 Electrolysis: Challenges and Untapped Opportunities. ACS Catal. *12*, 1037–1051.
5. De Luna, P., Hahn, C., Higgins, D., Jaffer, S.A., Jaramillo, T.F., and Sargent, E.H. (2019). What would it take for renewably powered electrosynthesis to displace petrochemical processes? Science *364*, eaav3506.
6. Andreoli, E. (2021). CO_2-to-ethylene electroreduction gets a boost. Nat. Catal. *4*, 8–9.
7. Sa, Y.J., Lee, C.W., Lee, S.Y., Na, J., Lee, U., and Hwang, Y.J. (2020). Catalyst–electrolyte interface chemistry for electrochemical CO_2 reduction. Chem. Soc. Rev. *49*, 6632–6665.
8. Hernandez-Aldave, S., and Andreoli, E. (2020). Fundamentals of Gas Diffusion Electrodes and Electrolysers for Carbon Dioxide Utilisation: Challenges and Opportunities. Catalysts *10*, 713.
9. Edwards, J.P., Xu, Y., Gabardo, C.M., Dinh, C.T., Li, J., Qi, Z.B., Ozden, A., Sargent, E.H., and Sinton, D. (2020). Efficient electrocatalytic conversion of carbon dioxide in a low-resistance pressurized alkaline electrolyzer. Appl. Energy *261*, 1–7.
10. Rabinowitz, J.A., and Kanan, M.W. (2020). The future of low-temperature carbon dioxide electrolysis depends on solving one basic problem. Nat. Commun. *11*, 5231.
11. Larrazábal, G.O., Strøm-Hansen, P., Heli, J.P., Zeiter, K., Therkildsen, K.T., Chorkendorff, I., and Seger, B. (2019). Analysis of Mass Flows and Membrane Cross-over in CO_2 Reduction at High Current Densities in an MEA-Type Electrolyzer. ACS Appl. Mater. Interfaces *11*, 41281–41288.
12. Ozden, A., Li, J., Kandambeth, S., Li, X., Liu, S., Shekhah, O., Ou, P., Zou Finfrock, Y.Z., Wang, Y., Alkayyali, T., et al. (2023). Energy- and carbon-efficient CO_2/CO electrolysis to multicarbon products via asymmetric ion migration-adsorption. Nat. Energy *8*, 179–190.
13. Ozden, A., Wang, Y., Li, F., Luo, M., Sisler, J., Thevenon, A., Rosas-Hernández, A., Burdyny, T., Lum, Y., Yadegari, H., et al. (2021). Cascade CO_2 electroreduction enables efficient carbonate-free production of ethylene. Joule *5*, 706–719.
14. Rabiee, H., Heffernan, J.K., Ge, L., Zhang, X., Yan, P., Marcellin, E., Hu, S., Zhu, Z., Wang, H., and Yuan, Z. (2023). Tuning flow-through Cu-based hollow fiber gas-diffusion electrode for high-efficiency carbon monoxide (CO) electroreduction to C_{2+} products. Appl. Catal. B *330*, 122589.
15. Kwon, S., Zhang, J., Ganganahalli, R., Verma, S., and Yeo, B.S. (2023). Enhanced Carbon Monoxide Electroreduction to >1 A cm^{-2} C_{2+} Products Using Copper Catalysts Dispersed on MgAl Layered Double Hydroxide Nanosheet House-of-Cards Scaffolds. Angew. Chem. Int. Ed. Engl. *62*, e202217252.
16. Zhao, C., Luo, G., Liu, X., Zhang, W., Li, Z., Xu, Q., Zhang, Q., Wang, H., Li, D., Zhou, F., et al. (2020). In Situ Topotactic Transformation of an Interstitial Alloy for CO Electroreduction. Adv. Mater. *32*, e2002382.
17. Duong, H.P., Tran, N.H., Rousse, G., Zanna, S., Schreiber, M.W., and Fontecave, M. (2022). Highly Selective Copper-Based Catalysts for Electrochemical Conversion of Carbon Monoxide to Ethylene Using a Gas-Fed Flow Electrolyzer. ACS Catal. *12*, 10285–10293.
18. Lu, X., Shinagawa, T., and Takanabe, K. (2023). Product Distribution Control Guided by a Microkinetic Analysis for CO Reduction at High-Flux Electrocatalysis Using Gas-Diffusion Cu Electrodes. ACS Catal. *13*, 1791–1803.
19. Li, J., Wang, Z., McCallum, C., Xu, Y., Li, F., Wang, Y., Gabardo, C.M., Dinh, C., Zhuang, T., Wang, L., et al. (2019). Constraining CO coverage on copper promotes high-efficiency ethylene electroproduction. Nat. Catal. *2*, 1124–1131.
20. Jouny, M., Luc, W., and Jiao, F. (2018). High-rate electroreduction of carbon monoxide to multi-carbon products. Nat. Catal. *1*, 748–755.
21. Ripatti, D.S., Veltman, T.R., and Kanan, M.W. (2019). Carbon Monoxide Gas Diffusion Electrolysis that Produces Concentrated C_2 Products with High Single-Pass Conversion. Joule *3*, 240–256.
22. Rabinowitz, J.A., Ripatti, D.S., Mariano, R.G., and Kanan, M.W. (2022). Improving the Energy Efficiency of CO Electrolysis by Controlling Cu Domain Size in Gas Diffusion Electrodes. ACS Energy Lett. *7*, 4098–4105.
23. Tran, N.H., Duong, H.P., Rousse, G., Zanna, S., Schreiber, M.W., and Fontecave, M. (2022). Selective Ethylene Production from CO_2 and CO Reduction via Engineering Membrane Electrode Assembly with Porous Dendritic Copper Oxide. ACS Appl. Mater. Interfaces *14*, 31933–31941.
24. Yadegari, H., Ozden, A., Alkayyali, T., Soni, V., Thevenon, A., Rosas-Hernández, A., Agapie, T., Peters, J.C., Sargent, E.H., and Sinton, D. (2021). Glycerol Oxidation Pairs with Carbon Monoxide Reduction for Low-Voltage Generation of C_2 and C_3 Product Streams. ACS Energy Lett. *6*, 3538–3544.
25. Li, J., Xu, A., Li, F., Wang, Z., Zou, C., Gabardo, C.M., Wang, Y., Ozden, A., Xu, Y., Nam, D.H., et al. (2020). Enhanced multi-carbon alcohol electroproduction from CO via modulated hydrogen adsorption. Nat. Commun. *11*, 3685.
26. Wu, F., Argyle, M.D., Dellenback, P.A., and Fan, M. (2018). Progress in O_2 separation for oxy-fuel combustion–A promising way for cost-effective CO_2 capture: A review. Prog. Energy Combust. Sci. *67*, 188–205.
27. Kibria Nabil, S.K., McCoy, S., and Kibria, M.G. (2021). Comparative Life Cycle Assessment of Electrochemical Upgrading of CO_2 to Fuels and Feedstocks. Green Chem. *23*, 867–880.
28. Jouny, M., Hutchings, G.S., and Jiao, F. (2019). Carbon monoxide electroreduction as an emerging platform for carbon utilization. Nat. Catal. *2*, 1062–1070.
29. Hauch, A., Küngas, R., Blennow, P., Hansen, A.B., Hansen, J.B., Mathiesen, B.V., and Mogensen, M.B. (2020). Recent advances in solid oxide cell technology for electrolysis. Science *370*, eaba6118.
30. Küngas, R. (2020). Review—Electrochemical CO2 Reduction for CO Production: Comparison of Low- and High-Temperature Electrolysis Technologies. J. Electrochem. Soc. *167*, 44508.
31. Ozden, A., García de Arquer, F.P., Huang, J.E., Wicks, J., Sisler, J., Miao, R.K., O'Brien, C.P., Lee, G., Wang, X., Ip, A.H., et al. (2022). Carbon-efficient carbon dioxide electrolysers. Nat. Sustain. *5*, 563–573.
32. Moore, T., Oyarzun, D.I., Li, W., Lin, T.Y., Goldman, M., Wong, A.A., Jaffer, S.A., Sarkar, A., Baker, S.E., Duoss, E.B., et al. (2023).

Electrolyzer energy dominates separation costs in state-of-the-art CO_2 electrolyzers: Implications for single-pass CO_2 utilization. Joule *7*, 782–796.

33. Zheng, Y., Wang, S., Pan, Z., and Yin, B. (2021). Electrochemical CO_2 reduction to CO using solid oxide electrolysis cells with high-performance Ta-doped bismuth strontium ferrite air electrode. Energy *228*, 120579.

34. Silva, G.F., Mendes, J.S., Mota, F.A.S., Ferreira, A.L.O., and Fernandes, F.A.N. (2010). Optimization of the Operating Conditions of Production Hydrogen from Glycerol Autothermal Reforming for fuel Cell. In 2nd International Conference on Engineering Optimization, pp. 1–5.

35. Lei, Y., Wang, Z., Bao, A., Tang, X., Huang, X., Yi, H., Zhao, S., Sun, T., Wang, J., and Gao, F. (2023). Recent advances on electrocatalytic CO_2 reduction to resources: Target products, reaction pathways and typical catalysts. Chem. Eng. J. *453*, 139663.

36. Gabardo, C.M., O'Brien, C.P., Edwards, J.P., McCallum, C., Xu, Y., Dinh, C.T., Li, J., Sargent, E.H., and Sinton, D. (2019). Continuous Carbon Dioxide Electroreduction to Concentrated Multi-carbon Products Using a Membrane Electrode Assembly. Joule *3*, 2777–2791.

37. Weng, L.-C., Bell, A.T., and Weber, A.Z. (2020). A systematic analysis of Cu-based membrane-electrode assemblies for CO_2 reduction through multiphysics simulation. Energy Environ. Sci. *13*, 3592–3606.

38. Weng, L.C., Bell, A.T., and Weber, A.Z. (2019). Towards membrane-electrode assembly systems for CO_2 reduction: A modeling study. Energy Environ. Sci. *12*, 1950–1968.

39. Weng, L.C., Bell, A.T., and Weber, A.Z. (2018). Modeling gas-diffusion electrodes for CO_2 reduction. Phys. Chem. Chem. Phys. *20*, 16973–16984.

40. McCallum, C., Gabardo, C.M., O'Brien, C.P., Edwards, J.P., Wicks, J., Xu, Y., Sargent, E.H., and Sinton, D. (2021). Reducing the crossover of carbonate and liquid products during carbon dioxide electroreduction. Cell Rep. Phys. Sci. *2*, 100522.

41. Dinh, C.T., Burdyny, T., Kibria, M.G., Seifitokaldani, A., Gabardo, C.M., García de Arquer, F.P., Kiani, A., Edwards, J.P., De Luna, P., Bushuyev, O.S., et al. (2018). CO_2 electroreduction to ethylene via hydroxide-mediated copper catalysis at an abrupt interface. Science *360*, 783–787.

42. Wu, K., Birgersson, E., Kim, B., Kenis, P.J.A., and Karimi, I.A. (2015). Modeling and Experimental Validation of Electrochemical Reduction of CO_2 to CO in a Microfluidic Cell. J. Electrochem. Soc. *162*, F23–F32.

43. Wang, X., Ou, P., Ozden, A., Hung, S.F., Tam, J., Gabardo, C.M., Howe, J.Y., Sisler, J., Bertens, K., García de Arquer, F.P., et al. (2022). Efficient electrosynthesis of n-propanol from carbon monoxide using a Ag–Ru–Cu catalyst. Nat. Energy *7*, 170–176.

44. Gerhardt, M.R., Pant, L.M., Bui, J.C.M., Crothers, A.R., Ehlinger, V.M., Fornaciari, J.C., Liu, J., and Weber, A.Z. (2021). Method—Practices and Pitfalls in Voltage Breakdown Analysis of Electrochemical Energy-Conversion Systems. J. Electrochem. Soc. *168*, 74503.

45. Salvatore, D., and Berlinguette, C.P. (2020). Voltage Matters When Reducing CO_2 in an Electrochemical Flow Cell. ACS Energy Lett. *5*, 215–220.

46. Vass, Á., Endrődi, B., and Janáky, C. (2021). Coupling electrochemical carbon dioxide conversion with value-added anode processes: an emerging paradigm. Curr. Opin. Electrochem. *25*, 100621.

47. Verma, S., Lu, S., and Kenis, P.J.A. (2019). Co-electrolysis of CO_2 and glycerol as a pathway to carbon chemicals with improved technoeconomics due to low electricity consumption. Nat. Energy *4*, 466–474.

48. Na, J., Seo, B., Kim, J., Lee, C.W., Lee, H., Hwang, Y.J., Min, B.K., Lee, D.K., Oh, H.S., and Lee, U. (2019). General technoeconomic analysis for electrochemical coproduction coupling carbon dioxide reduction with organic oxidation. Nat. Commun. *10*, 5193.

49. Medvedeva, X.V., Medvedev, J.J., Tatarchuk, S.W., Choueiri, R.M., and Klinkova, A. (2020). Sustainable at both ends: electrochemical CO_2 utilization paired with electrochemical treatment of nitrogenous waste. Green Chem. *22*, 4456–4462.

50. Ding, L., Zhu, N., Hu, Y., Chen, Z., Song, P., Sheng, T., Wu, Z., and Xiong, Y. (2022). Over 70 % Faradaic Efficiency for CO_2 Electroreduction to Ethanol Enabled by Potassium Dopant-Tuned Interaction between Copper Sites and Intermediates. Angew. Chem. Int. Ed. Engl. *61*, e202209268.

51. Sun, W., Wang, P., Jiang, Y., Jiang, Z., Long, R., Chen, Z., Song, P., Sheng, T., Wu, Z., and Xiong, Y. (2022). V-Doped Cu_2Se Hierarchical Nanotubes Enabling Flow-Cell CO_2 Electroreduction to Ethanol with High Efficiency and Selectivity. Adv. Mater. *34*, e2207691.

52. Wang, L., Nitopi, S.A., Bertheussen, E., Orazov, M., Morales-Guio, C.G., Liu, X., Higgins, D.C., Chan, K., Nørskov, J.K., Hahn, C., et al. (2018). Electrochemical Carbon Monoxide Reduction on Polycrystalline Copper: Effects of Potential, Pressure, and pH on Selectivity toward Multicarbon and Oxygenated Products. ACS Catal. *8*, 7445–7454.

53. Luo, M., Ozden, A., Wang, Z., Li, F., Erick Huang, J.E., Hung, S.F., Wang, Y., Li, J., Nam, D.H., Li, Y.C., et al. (2023). Coordination Polymer Electrocatalysts Enable Efficient CO-to-Acetate Conversion. Adv. Mater. *35*, e2209567.

54. Zhang, G., and Jiao, K. (2018). Multi-phase models for water and thermal management of proton exchange membrane fuel cell: A review. J. Power Sources *391*, 120–133.

55. Shahsavari, S., Desouza, A., Bahrami, M., and Kjeang, E. (2012). Thermal analysis of air-cooled PEM fuel cells. Int. J. Hydrog. Energy *37*, 18261–18271.

56. Adzakpa, K.P., Ramousse, J., Dubé, Y., Akremi, H., Agbossou, K., Dostie, M., Poulin, A., and Fournier, M. (2008). Transient air cooling thermal modeling of a PEM fuel cell. J. Power Sources *179*, 164–176.

57. Pribyl-Kranewitter, B., Beard, A., Schuler, T., Diklić, N., and Schmidt, T.J. (2021). Investigation and Optimisation of Operating Conditions for Low-Temperature CO_2 Reduction to CO in a Forward-Bias Bipolar-Membrane Electrolyser. J. Electrochem. Soc. *168*, 43506.

58. Aranguren, P., Astrain, D., Santa María, M., and Rojo, R. (2015). Computational study on a thermoelectric system used to dry out the hydrogen produced in an alkaline electrolyser. Appl. Therm. Eng. *75*, 984–993.

59. Yang, B., Liu, K., Li, H.J.W., Liu, C., Fu, J., Li, H., Huang, J.E., Ou, P., Alkayyali, T., Cai, C., et al. (2022). Accelerating CO_2 Electroreduction to Multicarbon Products via Synergistic Electric–Thermal Field on Copper Nanoneedles. J. Am. Chem. Soc. *144*, 3039–3049.

60. Herranz, J., Durst, J., Fabbri, E., Patru, A., Cheng, X., Permyakova, A.A., and Schmidt, T.J. (2016). Interfacial effects on the catalysis of the hydrogen evolution, oxygen evolution and CO_2-reduction reactions for (co-) electrolyzer development. Nano Energy *29*, 4–28.

61. Xing, Z., Hu, L., Ripatti, D.S., Hu, X., and Feng, X. (2021). Enhancing carbon dioxide gas-diffusion electrolysis by creating a hydrophobic catalyst microenvironment. Nat. Commun. *12*, 136.

62. Xu, Q., Garg, S., Moss, A.B., Mirolo, M., Chorkendorff, I., Drnec, J., and Seger, B. (2023). Identifying and alleviating the durability challenges in membrane-electrode-assembly devices for high-rate CO electrolysis. Nat. Catal. *6*, 1042–1051.

63. Yang, K., Kas, R., Smith, W.A., and Burdyny, T. (2021). Role of the Carbon-Based Gas Diffusion Layer on Flooding in a Gas Diffusion Electrode Cell for Electrochemical CO_2 Reduction. ACS Energy Lett. *6*, 33–40.

64. Karna, S.K., and Sahai, R. (2012). An overview on Taguchi Method. Int. J. Eng. Math. Sci. *1*, 11–18.

65. Qazi, M.I., Akhtar, R., Abas, M., Khalid, Q.S., Babar, A.R., and Pruncu, C.I. (2020). An integrated approach of GRA coupled with principal component analysis for multi-optimization of shielded metal arc welding (SMAW) process. Materials (Basel) *13*, 3457.

66. Tricker, A.W., Lee, J.K., Shin, J.R., Danilovic, N., Weber, A.Z., and Peng, X. (2023). Design and operating principles for high-performing anion exchange membrane water electrolyzers. J. Power Sources *567*, 232967.

67. Wang, X., Hu, Q., Li, G., Yang, H., and He, C. (2022). Recent Advances and Perspectives of Electrochemical CO_2 Reduction Toward C_{2+} Products on Cu-Based Catalysts. Electrochem. Energy Rev. *5*, 1–44.

68. Zang, Y., Wei, P., Li, H., Gao, D., and Wang, G. (2022). Catalyst Design for Electrolytic CO_2 Reduction Toward Low-Carbon Fuels and Chemicals. Electrochem. Energy Rev. *5*, 1–30.

69. Wu, D., Jiao, F., and Lu, Q. (2022). Progress and Understanding of CO_2/CO

Electroreduction in Flow Electrolyzers. ACS Catal. *12*, 12993–13020.

70. Hursán, D., and Janáky, C. (2023). Operando characterization of continuous flow CO_2 electrolyzers: current status and future prospects. Chem. Commun. (Camb) *59*, 1395–1414.

71. Kibria, M.G., Edwards, J.P., Gabardo, C.M., Dinh, C.T., Seifitokaldani, A., Sinton, D., and Sargent, E.H. (2019). Electrochemical CO_2 Reduction into Chemical Feedstocks: From Mechanistic Electrocatalysis Models to System Design. Adv. Mater. *31*, e1807166.

72. Garg, S., Li, M., Weber, A.Z., Ge, L., Li, L., Rudolph, V., Wang, G., and Rufford, T.E. (2020). Advances and challenges in electrochemical CO_2 reduction processes: An engineering and design perspective looking beyond new catalyst materials. J. Mater. Chem. A *8*, 1511–1544.

73. Tufa, R.A., Chanda, D., Ma, M., Aili, D., Demissie, T.B., Vaes, J., Li, Q., Liu, S., and Pant, D. (2020). Towards highly efficient electrochemical CO_2 reduction: Cell designs, membranes and electrocatalysts. Appl. Energy *277*, 115557.

74. Chen, X., Chen, J., Alghoraibi, N.M., Henckel, D.A., Zhang, R., Nwabara, U.O., Madsen, K.E., Kenis, P.J.A., Zimmerman, S.C., and Gewirth, A.A. (2021). Electrochemical CO_2-to-ethylene conversion on polyamine-incorporated Cu electrodes. Nat. Catal. *4*, 20–27.

75. Ma, W., Xie, S., Liu, T., Fan, Q., Ye, J., Sun, F., Jiang, Z., Zhang, Q., Cheng, J., and Wang, Y. (2020). Electrocatalytic reduction of CO_2 to ethylene and ethanol through hydrogen-assisted C–C coupling over fluorine-modified copper. Nat. Catal. *3*, 478–487.

76. Liu, M., Pang, Y., Zhang, B., De Luna, P., Voznyy, O., Xu, J., Zheng, X., Dinh, C.T., Fan, F., Cao, C., et al. (2016). Enhanced electrocatalytic CO_2 reduction via field-induced reagent concentration. Nature *537*, 382–386.

77. Burdyny, T., Graham, P.J., Pang, Y., Dinh, C.T., Liu, M., Sargent, E.H., and Sinton, D. (2017). Nanomorphology-Enhanced Gas-Evolution Intensifies CO_2 Reduction Electrochemistry. ACS Sustainable Chem. Eng. *5*, 4031–4040.

78. Li, D., Wu, J., Liu, T., Liu, J., Yan, Z., Zhen, L., and Feng, Y. (2019). Tuning the pore structure of porous tin foam electrodes for enhanced electrochemical reduction of carbon dioxide to formate. Chem. Eng. J. *375*, 122024.

79. Narayanaru, S., Anilkumar, G.M., Ito, M., Tamaki, T., and Yamaguchi, T. (2021). An enhanced electrochemical CO_2 reduction reaction on the SnO: X-PdO surface of SnPd nanoparticles decorated on N-doped carbon fibers. Catal. Sci. Technol. *11*, 143–151.

80. Albo, J., Perfecto-Irigaray, M., Beobide, G., and Irabien, A. (2019). Cu/Bi metal-organic framework-based systems for an enhanced electrochemical transformation of CO_2 to alcohols. J. CO2 Util. *33*, 157–165.

81. Thangavel, P., Ha, M., Kumaraguru, S., Meena, A., Singh, A.N., Harzandi, A.M., and Kim, K.S. (2020). Graphene-nanoplatelets-supported NiFe-MOF: high-efficiency and ultra-stable oxygen electrodes for sustained alkaline anion exchange membrane water electrolysis. Energy Environ. Sci. *13*, 3447–3458.

82. Luo, J.T., Zang, G.L., and Hu, C. (2020). An efficient 3D ordered mesoporous Cu sphere array electrocatalyst for carbon dioxide electrochemical reduction. J. Mater. Sci. Technol. *55*, 95–106.

83. Zhang, Y., Li, K., Chen, M., Wang, J., Liu, J., and Zhang, Y. (2020). Cu/Cu_2O Nanoparticles Supported on Vertically ZIF-L-Coated Nitrogen-Doped Graphene Nanosheets for Electroreduction of CO_2 to Ethanol. ACS Appl. Nano Mater. *3*, 257–263.

84. Wang, Y., Zhao, J., Cao, C., Ding, J., Wang, R., Zeng, J., Bao, J., and Liu, B. (2023). Amino-Functionalized Cu for Efficient Electrochemical Reduction of CO to Acetate. ACS Catal. *13*, 3532–3540.

85. Chen, X., Zhao, Y., Han, J., and Bu, Y. (2023). Copper-Based Catalysts for Electrochemical Reduction of Carbon Dioxide to Ethylene. ChemPlusChem *88*, e202200370.

86. Yang, K., Ni, H., Shui, T., Chi, X., Chen, W., Liu, Q., Xu, J., and Wang, Z. (2020). High conductivity and alkali-resistant stability of imidazole side chain crosslinked anion exchange membrane. Polymer *211*, 123085.

87. Hasa, B., Cherniack, L., Xia, R., Tian, D., Ko, B.H., Overa, S., Dimitrakellis, P., Bae, C., and Jiao, F. (2023). Benchmarking anion-exchange membranes for electrocatalytic carbon monoxide reduction. Chem. Catal. *3*, 100450.

88. Salvatore, D.A., Gabardo, C.M., Reyes, A., O'Brien, C.P., Holdcroft, S., Pintauro, P., Bahar, B., Hickner, M., Bae, C., Sinton, D., et al. (2021). Designing anion exchange membranes for CO_2 electrolysers. Nat. Energy *6*, 339–348.

89. Adnan, M.A., Shayesteh Zeraati, A.S., Nabil, S.K., Al-Attas, T.A., Kannimuthu, K., Dinh, C.-T., Gates, I.D., and Kibria, M.G. (2023). Directly-Deposited Ultrathin Solid Polymer Electrolyte for Enhanced CO_2 Electrolysis. Adv. Energy Mater. *13*, 2203158.

90. Veh, P., Britton, B., Holdcroft, S., Zengerle, R., Vierrath, S., and Breitwieser, M. (2020). Improving the water management in anion-exchange membrane fuel cells via ultra-thin, directly deposited solid polymer electrolyte. RSC Adv. *10*, 8645–8652.

91. Vierrath, S., Breitwieser, M., Klingele, M., Britton, B., Holdcroft, S., Zengerle, R., and Thiele, S. (2016). The reasons for the high power density of fuel cells fabricated with directly deposited membranes. J. Power Sources *326*, 170–175.

92. Ren, W., Ma, W., and Hu, X. (2023). Tailored water and hydroxide transport at a quasi-two-phase interface of membrane electrode assembly electrolyzer for CO electroreduction. Joule *7*, 2349–2360.

93. Grim, R.G., Ferrell, J.R., Huang, Z., Tao, L., and Resch, M.G. (2023). The feasibility of direct CO_2 conversion technologies on impacting mid-century climate goals. Joule *7*, 1684–1699.

94. Park, S., Grigioni, I., Alkayyali, T., Byoung-Hoon, L., Kim, J., Shirzadi, E., Dorakhan, R., Lee, G., Abed, J., Bossola, F., et al. (2023). High carbon efficiency in CO-to-alcohol electroreduction using a CO reservoir. Joule *7*, 2335–2348.

95. Weisenberger, S., and Schumpe, A. (1996). Estimation of Gas Solubilities in Salt Solutions at Temperatures from 273 K to 363 K. AIChE J. *42*, 298–300.

96. Sander, R. (2015). Compilation of Henry's law constants (version 4.0) for water as solvent. Atmos. Chem. Phys. *15*, 4399–4981.

97. Bohra, D., Chaudhry, J.H., Burdyny, T., Pidko, E.A., and Smith, W.A. (2019). Modeling the electrical double layer to understand the reaction environment in a CO_2 electrocatalytic system. Energy Environ. Sci. *12*, 3380–3389.

98. Singh, M.R., Goodpaster, J.D., Weber, A.Z., Head-Gordon, M., and Bell, A.T. (2017). Mechanistic insights into electrochemical reduction of CO_2 over Ag using density functional theory and transport models. Proc. Natl. Acad. Sci. USA *114*, E8812–E8821.

99. Weber, A.Z., and Newman, J. (2004). Modeling transport in polymer-electrolyte fuel cells. Chem. Rev. *104*, 4679–4726.

100. Weber, A.Z., and Newman, J. (2004). Transport in Polymer-Electrolyte Membranes: II. Mathematical Model. J. Electrochem. Soc. *151*, A311.

101. Peng, J., Roy, A.L., Greenbaum, S.G., and Zawodzinski, T.A. (2018). Effect of CO_2 absorption on ion and water mobility in an anion exchange membrane. J. Power Sources *380*, 64–75.

102. Kas, R., Yang, K., Yewale, G.P., Crow, A., Burdyny, T., and Smith, W.A. (2022). Modeling the Local Environment within Porous Electrode during Electrochemical Reduction of Bicarbonate. Ind. Eng. Chem. Res. *61*, 10461–10473.

103. Wilhelm, E., Battino, R., and Wilcock, R.J. (1977). Low-Pressure Solubility of Gases in Liquid Water. Chem. Rev. *77*, 219–262.